Lee, R. G., Byrne, K., D'Angelo, M., Hart, C. J., Hollings, P., Gleeson, S. A., Alfaro, M. (2021): Using zircon trace element composition to assess porphyry copper potential of the Guichon Creek batholith and Highland Valley Copper deposit, south-central British Columbia. - Mineralium Deposita, 56, 215-238.

https://doi.org/10.1007/s00126-020-00961-1

Using zircon trace element composition to assess porphyry copper potential of the Guichon Creek batholith and Highland Valley Copper deposit, south-central British Columbia

Robert G. Lee[1], Kevin Byrne[2,6], Michael D'Angelo[3], Craig J.R. Hart[1], Pete Hollings[3,] Sarah A. Gleeson[4,5], and Miguel Alfaro[6]

1. Mineral Deposit Research Unit, University of British Columbia, 2207-2020 Main Mall, Vancouver, British Columbia, V6T 1Z4
2. Department of Earth and Atmospheric Sciences, University of Alberta, Edmonton, Alberta, T6G 2E3, Canada
3. Geology Department, Lakehead University, 955 Oliver Rd, Thunder Bay, Ontario, P7B 5E1, Canada
4. GFZ German Research Centre for Geosciences, Telegrafenberg, 14473 Potsdam, Germany
5. Institute of Geological Sciences, Freie Universität Berlin, Malteserstrasse, 74-100, Berlin, 12249, Germany
6. Teck Resources Limited, Suite 3300, 550 Burrard Street, Vancouver, British Columbia, V6C 0B3, Canada

Corresponding author – rlee@eoas.ubc.ca

Abstract

The Late Triassic Guichon Creek batholith is a large (~1800 km^2), composite, zoned batholith that hosts several large porphyry Cu-Mo deposits of the Highland Valley Copper district. The batholith consists of intrusive rocks that range in composition from gabbro to quartz monzonite. Adjacent to the mafic margin of the batholith is the Gump Lake granodiorite to quartz monzonite stock. A new U-Pb zircon age of 218 ± 0.18 for the Gump Lake stock indicates that magmatism in the region began at least seven million years prior to the emplacement of the main Guichon Creek batholith rocks at 211 Ma.

Zircons from fifteen samples from the Guichon Creek batholith were analyzed by laser ablation ICP-MS to characterize the magmatic evolution and ore fertility of the batholith. The trace element composition of zircon record early, lower crustal, fractional crystallization followed by five pulses of magma recharge and mixing in an upper crustal, oxidized, magma chamber as well as degassing of the magmatic-hydrothermal fluids that formed the porphyry copper deposits. Zircons from the early barren rocks have chondrite-normalized Eu/Eu_N* values of 0.19 to 0.56 and estimated temperatures of 850 to 750 °C. The middle to late intrusions that host porphyry copper mineralization have zircon Eu/Eu_N* values of 0.30 to 0.74 and slightly lower estimated temperatures of 800 to 600 °C. Late porphyritic stocks and dikes from the mineralized centers contain zircon crystals elevated in Y, Nb, Ta, and REE concentration relative to zircon from the earlier intrusions. This distinct change in zircon composition coincides with the copper mineralization, suggesting that zircon chemistry can be used as a tool to identify the genetic evolution of a crystallizing magma chamber and potential for mineralization.

Introduction

50 It has been proposed that trace element concentrations in zircon can track the hydration
51 and oxidation state in magmas that produce economic ore deposits (Ballard et al. 2002; Wang et
52 al. 2014; Dilles et al. 2015; Lu et al. 2016). Several deposit-scale studies have shown that zircon
53 in rocks that are contemporaneous with mineralization have elevated Ce^{4+}/Ce^{3+} ratios and
54 Eu/Eu_N* values combined with distinctive Yb/Gd_N and Th/U ratios, as well as higher Y, Nb, and
55 Ta concentrations compared to barren igneous rocks (Liang et al. 2006; Wainwright et al. 2011;
56 Dilles et al. 2015; Shen et al. 2015; Lu et al. 2016; Banik et al. 2017; Lee et al. 2017b; Olson et
57 al. 2017; Large et al. 2018; Bouzari and Hart, 2019). Additionally, the chemical composition of
58 igneous rocks can be used to calculate zircon saturation temperatures, which potentially can
59 characterize magmatic cooling and potential heating by recharge events (Miller et al. 2003;
60 Watson et al. 2006; Lee et al. 2017b).

61 Porphyry copper deposits form from fluids exsolved from moderately oxidized, silica-
62 rich melts with high S, Cl, and water content (Dilles, 1987; Candela, 1992; Richards, 2003,
63 Seedorff et al. 2005; Sillitoe, 2010). Zircon that crystallizes in the intrusive rocks that form these
64 fluids record the oxidation state and conditions of the melt at the time of crystallization (Ballard
65 et al. 2001; Dilles et al., 2015). Anomalously high values of Ce and small negative Eu anomalies
66 in zircon are the result of elevated oxygen fugacity or high magmatic water content in the
67 crystallizing parental melt (Burnham et al. 2015; Smythe and Brenan, 2015). Elevated mean
68 Ce^{4+}/Ce^{3+} ratios and proxy Ce/Ce_N* values (Loader et al. 2017) greater than 100 have been
69 observed in numerous mineralized ore bodies whereas barren rocks typically have values that
70 range from 5 to 120 (Ballard et al. 2002; Liang et al. 2006; Wang et al. 2013; Lu et al. 2016;
71 Loader et al. 2017).

Zircon Eu/Eu_N^* ratios are potentially useful for characterization of magmas that form porphyry copper mineralization, with values greater than 0.4 observed in rocks that host or cause mineralization (Ballard et al. 2002, Wang et al. 2013; Dilles et al. 2015; Lee et al. 2017b). The Eu/Eu_N^* ratio has been proposed to be a proxy for either magmatic oxidation state (Shen et al. 2015; Lee et al. 2017b), or hydration state (Lu et al. 2016). A detailed evaluation of zircon composition can, thus, be used to identify rocks that could produce ore-forming mineralization as opposed to barren intrusions while also providing age constraints via the U-Th-Pb isotopic system.

The Late Triassic Guichon Creek batholith located in south-central British Columbia covers an area of 60 by 25 km and includes six intrusions that evolve from an older mafic margin inward to a younger and generally more felsic core (Fig. 1; McMillan, 1976; D'Angelo et al. 2017; Whalen et al. 2017). The batholith hosts the Highland Valley Copper (HVC) district with proven and probable reserves of 546 Mt @ 0.29% Cu and 0.008% Mo (Teck 2016 AIF, March 2017). Since production began in the early 1960s, the HVC district has produced over 1.6 GT of ore from the four primary porphyry deposits: Valley, Lornex, Highmont, and Bethlehem (Fig. 2; Byrne et al. 2013). The batholith additionally hosts over 160 mineralized showings and prospects (Fig. 1; Byrne et al. 2013, 2017). The large tonnage porphyry Cu systems are hosted within the youngest and more evolved intrusions in the core of the batholith.

A previous study on zircon chemistry in the Guichon Creek batholith identified elevated Ce^{4+}/Ce^{3+} values in four samples from the Bethlehem and Bethsaida facies of the batholith as well as the post-mineral Gnawed Mountain porphyry located in the core of the batholith (Ward, 2008). The current study utilizes an updated and detailed geological framework and evolution proposed by D'Angelo et al. (2017) to explore this relationship in more detail. We have analyzed

zircons from fifteen samples, including eight of the main rock types that were previously dated by CA-TIMS (ESM Table S1; D'Angelo et al. 2017), to assess the processes of fractional crystallization, recharge, and magma mixing, as well as their relationship to magma redox-state, water content and porphyry Cu formation. We investigate the genetic link between magmatic evolution and porphyry formation using zircon composition as a proxy for the oxidation state and composition of the magma by comparing the composition of zircon that crystallized from the early barren, though very weakly mineralized marginal rocks, to the younger well-mineralized rocks in the core of the batholith.

Regional Geology

The Late Triassic Guichon Creek batholith is located within the Intermontane belt of British Columbia and is composed of multiple intrusions of gabbro, diorite, granodiorite, and quartz monzonite that zone inwards from a mafic margin to a felsic core (Fig. 1; McMillan et al. 2009; D'Angelo et al. 2017). These igneous rocks intruded over approximately 4 Ma (D'Angelo et al. 2017) into an evolving and thickening upper-crustal magma chamber (Northcote, 1969; McMillan, 1976). The intrusive rocks were emplaced into volcanic and sedimentary rocks of the 238-202 Ma Nicola Group, an island-arc assemblage that makes up the southern part of the Quesnel terrane (Preto, 1979; Ray et al. 1996; Mortimer, 1987; Logan and Mihalynuk, 2014; Mihalynuk et al. 2016). The Guichon Creek batholith is magnetite-bearing, mostly metaluminous, calc-alkaline in composition, and one of several large Mesozoic plutonic bodies within southern British Columbia (Mortimer, 1986; McMillan, 1985; Ash et al. 2007; D'Angelo et al. 2017).

Five main intrusive facies make up the Guichon Creek batholith: the Border, Highland Valley, Bethlehem, Skeena, and Bethsaida facies. The Highland Valley facies is sub-divided into

the Guichon and Chataway subfacies. Numerous syn- to post-mineralization porphyritic to aplitic dikes and stocks cut the main intrusive facies with the highest density occurring primarily within and adjacent to the porphyry deposits (Fig. 2). Emplacement of the Guichon Creek batholith into the Nicola Group occurred in at least three pulses at depths of 4-5 km, with geophysical data suggesting it forms an elongate flattened body with a thickened core centered near the Bethlehem deposits (Ager et al. 1973; McMillan, 1985; Roy and Clowes, 2000; D'Angelo, 2016; D'Angelo et al. 2017). Based on cross-cutting relationships, whole-rock characteristics, and dating, D'Angelo et al. (2017) argued that the Guichon Creek batholith consists of three co-genetic pulses: (1) early (Border and Highland Valley facies), (2) middle (Bethlehem facies, dikes and stocks), and (3) late (Skeena and Bethsaida facies) with the Skeena facies potentially the result of mixing in the upper crustal magma chamber between the melt that formed Bethlehem facies and the melt that formed the Bethsaida facies.

Hydrothermal alteration of the Highland Valley deposits consists of multiple generations of fluid flow originating at the core of the batholith with two mineralizing events occurring at ~209 & 208 Ma (Casselman et al. 1995; Byrne et al. 2013; Byrne et al. 2017; D'Angelo et al. 2017). Copper and molybdenum sulfide ores formed in a high-temperature assemblage of K-feldspar, biotite, and early coarse-grained muscovite, overprinted by a lower temperature assemblage of fine-grained white mica, chlorite, and carbonate (Lesage et al. 2016; 2019). Alteration types that occur peripheral to Cu mineralization, and are present across the region in variable intensities, consist of sodic-calcic (albite-epidote-actinolite) and propylitic (epidote-chlorite-prehnite ± pumpellyite ± carbonate) assemblages (Byrne et al. 2017). Mineralization primarily occurs in quartz veins and as fracture fills with muscovite alteration halos within the Bethsaida facies of the larger Valley-Lornex-Highmont deposit. An older mineralization event at

Bethlehem occurs as mineralized breccias as well as disseminated chalcopyrite ± bornite in the Bethlehem intrusions, stocks, and porphyritic dike (McMillan, 1976; Casselman et al. 1995; Byrne et al. 2013).

Methodology

Zircons were separated from fifteen samples within the Guichon Creek batholith region, including the Gump Lake stock; the Border, Highland Valley, Bethlehem, Skeena, and Bethsaida facies; and samples of pre-, syn-, and post-mineralization stocks and dikes from the main pits of the Highland Valley Copper deposits (Fig. 2). Detailed petrology descriptions, geochemical data, U/Pb CA-TIMS ages, and paragenesis of the rock samples are discussed in detail by D'Angelo et al. (2017) and summarized below. One additional sample of the Gump Lake stock has been analyzed for U/Pb zircon age and trace element composition for this study. Samples selected from D'Angelo et al.'s (2017) suite for this study were fresh or weakly altered; however, due to the high intensity of alteration closer to the main ore bodies, many of the rock samples contained small fractures with alteration halos. Consequently, all zircon grains analyzed in this study were carefully characterized via petrography and cathodoluminescence imaging to determine if any hydrothermal overprint, identified by mottled internal zoning, highly luminescent rinds, and elevated LREE composition was evident. No extensively altered zircon crystals were observed during this study.

Whole-rock analysis

Whole-rock analyses were undertaken at ACME Analytical Laboratory (now Bureau Veritas Laboratories), Vancouver, Canada. A two-gram sample split was mixed with 1.5 grams of lithium metaborate/tetraborate mixture and fused at 1000 °C. The cooled bead was then

digested in 100 mL of 5% HNO_3, and the subsequent solution was analyzed for major and minor elements by inductively coupled plasma atomic emission spectroscopy (ICP-AES), and for trace elements by inductively coupled plasma mass spectrometry (ICP-MS). Loss on ignition (LOI) is reported as % weight loss on a one gram split ignited at 1000 °C. Wet chemical titration was used to measure FeO concentrations at Activation Laboratories Ltd. (ActLabs) in Ontario, Canada. Analytical details and uncertainties are presented in D'Angelo et al. (2017); results from samples used in this study are presented in the ESM Table S2 and D'Angelo et al. (2017).

Zircon grain selection

Zircons were separated from samples by crushing, grinding, and Wilfley table techniques, and individual grains were then handpicked under a binocular microscope. Grains selected for the study ranged from 100 μm to 200 μm in length, were generally euhedral in shape, and varied in color from colorless to light rose pink. All three hundred grains collected for laser ablation analysis were photographed, and spots were selected to avoid visible inclusions and defects in the grain (Fig. 3). Potential resorbed, inherited cores were observed in a few of the grains analyzed, but were generally rare. Both core and rim analyses were conducted where possible to test for zoning of age and trace elements.

U-Pb Geochronology

Zircons from the Gump Lake stock (sample KB132), which has not been previously dated, were analyzed by the CA-TIMS method at the Pacific Centre for Isotopic and Geochemical Research (PCIGR) at the University of British Columbia, Vancouver, B.C. The zircon grains were annealed and placed in baths of HF and HNO_3 acid and then dried for analysis following procedures modified from Mundil et al. (2004), Mattinson (2005), and Scoates and

Friedman (2008). Isotopic ratios were measured using a modified single collector VG-54R thermal ionization mass spectrometer equipped with an analog Daly photomultiplier. Analytical measurements are presented in Table 1, and detailed methods and results for U-Pb dating for the other samples in this study are given in D'Angelo et al. (2017). Additional zircon grains from these samples were analyzed for trace element composition.

Laser ablation inductively coupled plasma mass spectrometer analyses

Approximately twenty zircon grains were picked from each sample, mounted in epoxy pucks, and photographed under reflected and transmitted light, both before and after laser analysis, using a high-powered binocular microscope. The photographs were used to identify any melt and mineral inclusions as well as any grain defects (Fig. 3; ESM Fig. S1). Cathodoluminescence imaging was conducted using a Robinson cathodoluminescence detector mounted on a Philips XL-30 scanning electron microscope (SEM) at the University of British Columbia Electron Microbeam & X-Ray Diffraction Facility using 3 nA beam current and 20 kV accelerating voltage. All zircon trace element compositions were analyzed using a RESOlution M-50LR laser attached to an Agilent 7700 Series quadrupole inductively coupled plasma mass spectrometer (ICP-MS) at PCIGR. An ablation spot size of 47 μm was used for all grains. Twenty-nine isotope masses were analyzed for this study and results are presented in ESM Table S3. During the analytical run zircon age standards and trace element standards bracketed eight to ten unknown analyses: 91500 (Wiedenbeck et al. 2004), Plešovice (Sláma et al. 2008), Temora (Black et al. 2003), and standard trace element reference materials: NIST-610, NIST-612, and BCR-2G. Calibration of trace element concentrations was done using NIST-612 as the external standard and Zr as the internal standard due to the high concentration in zircon and cross-checked with NIST-610 and BCR-2G for quality control. Data reduction and processing were

done using the Iolite software package (Paton et al. 2011). All standard analytical measurements are within two standard deviations of accepted values, and full results are presented in ESM Table S3. Zircon trace element composition, normalized REE values, and calculated values used in this study are presented in ESM Table S4.

Analyses with concentrations of Ca > ~300 ppm and anomalous La values > 1 ppm were assumed to have ablated mineral (apatite) and melt inclusions, and these data were discarded (eight percent of the 450 analytical measurements were excluded). The REE concentrations were normalized to chondrite values of Anders and Grevesse (1989) multiplied by 1.3596 after Mazdab and Wooden (2006). Normalized values of Ce_N, Nd_N, Sm_N, Eu_N, and Gd_N were used to calculate Ce/Ce_N^* ($=Ce_N \div [(Nd_N)^2 \div Sm_N]$; Loader et al. 2017) and Eu/Eu_N^* ($Eu_N \div [Sm_N * Nd_N]^{1/2}$; Dilles et al. 2015). Exponential power function, as described by Zhong et al. (2019), was used to calculate Ce/Ce_C^* values and calculations are presented in ESM Table S5.

Sample description and major element composition

Gump Lake stock: The Gump Lake stock is granodioritic to quartz monzonitic in composition and covers an area of 23 km^2 along the eastern edge of the Guichon Creek batholith (Fig. 2; Northcote, 1969). Sample KB132, collected near the contact with the Border facies and Nicola Group (Fig. 2), is a medium- to coarse-grained equigranular quartz monzonite. The sample was relatively fresh; however, fine ≤1 mm veinlets of epidote+chlorite±tourmaline were present. The Gump Lake stock is geochemically distinct from the early Guichon Creek batholith intrusions due to higher SiO_2 and lower Al_2O_3, Fe_2O_3, and MgO contents, but has similar trace element compositions (Fig. 4).

Early Border and Highland Valley facies: The earliest intrusion of the Guichon Creek batholith is the Border facies, a heterogeneous body that includes olivine leuco-gabbro, olivine leuco-monzogabbro, diorite, quartz diorite, and quartz monzodiorite (D'Angelo et al. 2017). Amphibole is common in these rocks with abundant clinopyroxene and orthopyroxene in the more mafic rocks. Accessory minerals include magnetite, biotite, apatite, titanite, zircon, and rutile (D'Angelo et al. 2017). The Border facies locally contains xenoliths of Nicola Group as well as autoliths of the various rock types that occur within the Border facies. The Border facies has the most variable compositions of the main intrusions with SiO_2 contents varying from ~46 to 60 wt.% (Fig. 4A). Sample SB123 is an equigranular medium-grained gabbro collected 7 km southwest of the Lornex pit. The sample differs in chemical composition from the other intrusive samples, and has lower concentrations of large ion lithophile elements and higher concentrations of high field strength elements, except for Zr and Hf (Fig. 4D). The magmas that produced the Border facies likely assimilated some Nicola Group and other crust (D'Angelo et al. 2017); nonetheless, the Border facies represents the most primitive composition of magma; therefore, its zircon compositions are compared below with those of later and more evolved intrusions.

The Border facies is in contact with the equigranular granodiorites of the Highland Valley facies, which is further divided into the Guichon and Chataway subfacies, as well as a transitional phase between the two. Contacts between the two subfacies are gradational throughout the batholith and have been distinguished mainly by mineralogical and textural differences (McMillan 1976, 1985; Byrne et al. 2013). One sample of the Guichon subfacies (SM059) was collected from the west wall of the Bethlehem pit, and samples of the Chataway subfacies (MA026 and MA038) were collected from the east and west sides of the batholith (Fig.

2). All three samples overlap in age (ESM Table S1) and composition (Fig. 4). Sample MA038, collected near a transitional zone between the two subfacies, has higher Zr content and lower molar Al/Ti compared with MA026 (Fig. 4B), although both samples show similar textures and rock composition of hornblende-biotite-phyric quartz diorite to granodiorite (D'Angelo et al. 2017). The zircon composition of the two samples is distinct (see below) and, thus, MA038 is termed Guichon-Chataway transition for clarity.

Bethlehem facies and dikes from Bethlehem pit: The contacts between the early 211.0 ± 0.17 to 210.4 ± 0.41 Ma intrusive rocks and the Bethlehem facies vary from gradational to sharply cross-cutting, and in exposures in the Bethlehem Mine, the contact between the Bethlehem and Guichon subfacies is sharp (Carr, 1966; Byrne et al. 2013). The Bethlehem facies is a granodiorite and varies from equigranular to weakly porphyritic. Two samples were collected for this study: SM058 is a hornblende-phyric granodiorite from the southern section of the Bethlehem pit, and MA099 is a hornblende-phyric granodiorite collected north of the Valley pit (Fig. 2).

In the Guichon Creek batholith concentrations of Al_2O_3, TiO_2, and Zr have been used to characterize the different rock units due to the immobility of these phases (Byrne et al. 2013; D'Angelo et al. 2017). The chemical composition of the Bethlehem facies marks the distinct break between the early intrusive facies and younger Guichon Creek batholith facies with differing trends in SiO_2 vs. Al_2O_3 and Zr vs. molar Al/Ti as well as lower REE and trace element concentrations (Fig. 4). The early intrusions have low Al/Ti_{molar} values (<50), whereas the later intrusions and dikes have higher Al/Ti_{molar} values (>80), and the Bethlehem facies have values between the two (Fig. 4B).

The highest concentration of dikes in the Highland Valley Copper district are found within, and proximal to, the Bethlehem pit and based on mapped geological contacts, drill core logging, and age dating, the Bethlehem deposit is interpreted to have formed prior to the Valley-Lornex-Highmont deposits (McMillan, 1985; Byrne et al. 2013; D'Angelo et al. 2017). Zircons were collected from three dikes in the Bethlehem pit, from drill core and bench face, to compare the zircon compositions of Bethlehem dikes with other intrusive rocks (Fig. 2, inset). Sample SM056 was collected from the northern wall of the Bethlehem pit and is a porphyritic variety of the Bethlehem facies that pre-dates mineralization. Sample SM060 was collected from drill core in the Bethlehem pit and is a quartz-feldspar phyric porphyry termed the Late Jersey Stock that is inter- to post-mineralization. The final sample (SM057) was collected in the center of the Bethlehem pit and is a feldspar and quartz-phyric crowded porphyry (FQPC) that is late- to post-mineralization. Accessory mineral phases are the same within the Bethlehem rocks and the later facies in the Guichon Creek batholith, and include titanite, apatite, and rutile along with zircon, with magnetite abundance decreasing in the younger facies (Byrne et al. 2013; D'Angelo et al. 2017).

Late Guichon Creek intrusions and dikes: The youngest of the main Guichon Creek batholith intrusions include the Skeena facies, a seriate granodiorite with subordinate monzogranite, and the Bethsaida facies, a weakly porphyritic granodiorite to monzogranite. Contacts between the Skeena and Bethsaida facies with the Bethlehem facies are gradational over multiple meters and have been interpreted to reflect progressive crystallization of a single magma (McMillan, 1985) or alternatively, mixing between separate Bethlehem and Bethsaida magmas (D'Angelo et al. 2017). One sample of Skeena facies (SM055) collected from the Highmont pit is an equigranular biotite-hornblende granodiorite. Two samples of the Bethsaida facies were

297 collected and consist of quartz-biotite-phyric quartz monzonite to granodiorite. Sample SB217
298 was collected west of the Valley pit, and SB218 was collected south of the Lornex pit (Fig. 2).

299 A sample (SM061) of the quartz-biotite-phyric quartz monzonite to granodiorite stock
300 defined as the 'salt and pepper' ("S&P") Bethsaida was collected from drill core within the
301 Valley pit. The sample differs from the Bethsaida facies in its textural appearance of speckled
302 biotite (5-10%) and equant plagioclase (25%) grains (Byrne et al. 2013) as well as chemical
303 composition (Fig. 4). Cross-cutting relationships indicate that the "S&P" Bethsaida intrudes into
304 the Bethsaida facies. Barren quartz veins and a few quartz-muscovite-sulfide veins cut the dike,
305 which suggests it is pre- to syn-mineral.

306 A post-mineral quartz-feldspar-phyric, quartz-rich, porphyry dike with an aplitic
307 groundmass (QFPQ) was collected from the Highmont Pit (Fig. 2; MA121). The QFPQ is an
308 elongate east-west dike located in the Highmont area of the HVC district (Fig. 2) and represents
309 a late porphyry intrusion that is compositionally similar to and has similar zircon composition to
310 the melt which formed the "S&P" Bethsaida (Fig. 3; see below). Phenocrysts of partially
311 resorbed quartz 'eyes' (15-25%) and plagioclase (20%) occur within an aplitic groundmass of K-
312 feldspar, plagioclase, and quartz with <5% biotite and rare accessory titanite, apatite, rutile, and
313 zircon (D'Angelo et al. 2017). The sample has the youngest U-Pb age (206.95±0.22 Ma) of all
314 dated samples in the region (Ash et al. 2007; D'Angelo et al. 2017). The dike intrudes the
315 Skeena facies and appears to post-date all mineralization in the Lornex and Highmont pits
316 (Byrne et al., 2013; D'Angelo et al., 2017). The sample has the highest Al/Ti_{molar} ratio and
317 lowest LREE contents relative to all other samples collected for this study (Fig. 4). The late
318 post-mineral dike, as well as the "S&P" Bethsaida and the Bethlehem porphyry, are the only
319 samples to have a significant negative europium anomaly (Fig. 4C).

Results

U-Pb geochronology

Ages of the main Guichon Creek batholith samples used in this study range from 211.02 ± 0.17 to 206.95 ± 0.22 Ma (ESM Table S1). Zircon crystals from the Gump stock were analyzed using the same high precision U-Pb method, and results from the five analyses are presented in Table 1. The isochron ages plotted in Figure 5 illustrate that all individual analyses are concordant and have $^{206}Pb/^{238}U$ ages ranging from 219.12 ± 0.62 to 217.96 ± 0.24 Ma. The three older ages are interpreted to be older antycrysts, and the weighted average of the two youngest concordant fractions yielded an age of 218.01 ± 0.18 Ma (±2s; MSWD = 0.47) which we use as the best estimate of the crystallization age of the sample.

Zircon compositions

Gump Lake stock and early intrusions: The zircons from the Border and Highland Valley facies are distinct from those of the younger rocks having a higher percentage of grains with sector growth zoning. Zircon crystals from the Guichon Creek batholith rocks are characterized by a higher percentage of concentric or oscillatory growth zones that are typical of normal magmatic crystallization (Fig. 3; Vavra, 1994; Hoskin and Schaltegger, 2003). Zircon from the Gump Lake Stock contained a high density of inclusions (Fig. 3a-c) and although analytical spots were chosen to avoid these inclusions, only eight spots provided analytically viable trace element results after culling anomalous data (ESM Table S3). The Gump Lake stock has the least variable Hf content of all the samples (9160-9630 ppm), and Eu/Eu_N^* values less than 0.4 (Fig. 6A). The early Border facies has Eu/Eu_N^* values of 0.30 to 0.55, whereas the Guichon and Guichon-Chataway subfacies have Eu/Eu_N^* values that range from 0.20 to 0.40 (Fig. 6B). The

342 Chataway subfacies (MA026) zircon cores have Eu/Eu_N^* values of 0.32 to 0.46, whereas the
343 rims ranged from 0.33 to 0.72 and have higher Hf contents.

344 Zircon crystallization temperatures were calculated using the Ti-in-zircon thermometer of
345 Watson et al. (2006), assuming SiO_2 and TiO_2 activities of 1.0 and 0.7, respectively due to the
346 presence of quartz and Ti-bearing minerals (Ferry and Watson, 2007; Hayden and Watson,
347 2007). Estimated temperatures for all samples range from 954 to 597 ± 15°C (ESM Table S4).
348 The Border facies differs from the other samples as it has SiO_2 of 49.9 wt.% yielding an
349 underestimated zircon saturation temperature of ~600° C (ESM Table S2). For the Ti-in-zircon
350 estimate, while the sample does contain rutile lower activities of 0.5 have been used to estimate
351 temperature (Hayden and Watson, 2007). Zircon from the early Border facies and Highland
352 Valley facies generally have higher Ti content and higher estimated temperatures that range from
353 850 to 700 °C; however, the Gump Lake stock differs with temperature estimates of 733 to 660
354 °C (Fig. 7A).

355 Middle Bethlehem facies and Bethlehem dikes: Zircon from both the equigranular and
356 porphyritic dikes and stocks of the Bethlehem facies all have similar grain morphologies (ESM
357 Figure S1) and similar trace element compositions (Table 3). The Bethlehem facies zircons all
358 have $Eu/Eu_N^* > 0.35$ at Hf > 8,000 ppm (Fig. 6C). Most zircons have Hf values between 8,000
359 and 11,000 ppm, but those from the Bethlehem porphyry (SM056) and the late Jersey Stock
360 (SM060) at the Bethlehem Mine have higher values, up to 13,370 ppm (Fig. 6D). Ti-in-zircon
361 temperatures for the middle Guichon Creek batholith samples range from 800 to 600 °C although
362 there is one outlier in the Bethlehem facies at 900 °C (Fig. 7B).

Late Skeena and Bethsaida: Zircons from the Skeena and Bethsaida facies are generally euhedral with oscillatory growth zoning and contain variable numbers of inclusions (Fig. 3G-I). The Skeena and Bethsaida facies have zircon compositions similar to the middle Guichon Creek batholith samples and have $Eu/Eu_N^* > 0.39$ (Fig. 6E) and temperatures ranging from 784 to 610 °C (Fig. 7C). Zircons from the Skeena and Bethsaida samples and the earlier intrusions have similar Y, Nb/Ta, and REE compositions (Figs. 8, 9).

Syn- to post-mineral dikes: Zircons from the late syn-mineral "S&P" Bethsaida stock and post-mineral QFPQ dike have higher concentrations of Y and higher Nb/Ta ratios compared to zircon from the older samples (Fig. 8). Additionally, zircon REE concentrations in these dikes display distinct differences, with increased Ce_N and Yb_N contents compared to the other samples (Fig. 9). The Eu/Eu_N^* values decrease (0.70 to 0.20) with increasing Hf content (Fig. 6F) and have calculated Ti-temperatures that range from 800 to 600 °C (Fig. 7D).

Discussion

Trace element chemical evolution in the Guichon Creek batholith zircons

Growth zoning of zircon in calc-alkaline magmas is dependent on several factors, including fluid saturation and trace element concentration within the melt (Varva, 1994; Hanchar and Watson, 2003). Inclusions of melt and accessory mineral grains such as apatite, titanite, and high rare earth element (REE) bearing minerals can be common (Thomas et al. 2003; Lu et al. 2016; Lee et al. 2017b; Loader et al. 2017). Detailed characterization of zircon crystals is paramount because the analysis of inclusions can affect the light REE (LREE) and middle REE (MREE) concentrations, as both apatite and titanite preferentially incorporate LREE and MREE (Sha and Chappell, 1999; Colombini et al. 2011) compared to zircon, which contains relatively

low contents of LREE (Hanchar and van Westrenen, 2007). Apatite inclusions, as well as melt inclusions, were observed within the zircon crystals from the Guichon Creek rocks (Fig. 3), suggesting ongoing crystallization of both during the crystallization of the melt. Inclusions were avoided when analyzing for the zircon trace element concentration to avoid contamination.

Trace element concentrations of Hf, Y, REE, Th, and U in zircon can be used to track magmatic evolution and the roles of crystal fractionation or mixing (Gagnevin et al. 2010; Lee et al., 2017). Hafnium content in zircon can also be used as a proxy for magmatic crystallization, particularly zircon crystallization, because Hf increases in the melt due to its incompatibility and because crystallizing zircon has a Zr/Hf ratio greater than melt (Claiborne et al. 2006; Watson et al. 2006; Wooden et al. 2006; Dilles et al. 2015; Lee et al. 2017b). Cerium and Yb concentrations of zircon from the early to late intrusions of the Guichon Creek batholith increase (Fig. 9) as the magmas evolve to more felsic compositions with time (Fig. 4). An increase in Yb/Gd_N ratio (from 12 to 45) accompanying a decrease in Sm/Ce_N ratio (from 2 to 0.2) is consistent with fractional crystallization of MREE (Gd, Sm)-rich amphibole in the early magmas (Fig. 10B). Preferential removal of MREE by fractional crystallization of amphibole ± apatite ± titanite will increase Yb/Gd_N ratios of melt and crystallized zircon (Lee et al. 2017b; Loader et al. 2017), this process may be responsible for the higher Yb/Gd_N (20-45) zircon rims compared to cores (Hanchar and van Westrenen 2007; Lee et al. 2017b; Olson et al. 2017). Low Yb/Gd_N ratios and HREE contents have been observed in studies of porphyries from other localities that have undergone garnet fractionation in the lower crust (Bissig et al. 2017); there is no evidence that deep garnet fractionation occurred in the Guichon Creek batholith. The LREE fractionated whole rock patterns are consistent with the dominance of amphibole fractionation (Fig. 4C; D'Angelo et al. 2017).

The zircon from late-intrusions and syn- to post-mineral dikes have elevated Yb/Gd_N values (>20) suggesting apatite and titanite, along with amphibole, played a significant role in magma formation as they preferentially incorporate LREE and MREE (Fig. 10A; see also Sha and Chappell, 1999; Colombini et al. 2011; Olson et al. 2017). Amphibole is a common mineral phase in the early to mid-facies of the Guichon Creek batholith granodiorite rocks, while both apatite and titanite increase as accessory phases in the younger samples (Byrne et al. 2013; D'Angelo et al. 2017). Titanite is generally stable at temperatures below 780 °C (Dilles, 1987; Piccoli et al. 2000; Olson et al. 2017), and minor fractionation of titanite can depress the REE content within a hydrous melt (Loader et al. 2017; Olson et al. 2017). The calculated Ti-in-zircon temperatures for the Guichon Creek rocks fall within the temperature field where titanite will crystallize (Fig. 7), and the REE ratios of zircon are consistent with amphibole, apatite, and titanite crystallization. The presence of apatite (Fig. 3) and titanite inclusions in the zircon support this hypothesis.

Ratios of Hf/Y and Th/U of zircon are also consistent with an evolving magmatic system from early amphibole-dominated fractionation to amphibole plus apatite and titanite (Fig. 10). As melt evolves to more silicic compositions, the concentrations of U, Th, and Y generally increase, and Th/U ratio typically decreases in zircon (Clairborne et al. 2006; 2010; Gagnevin et al. 2010). In mafic to intermediate magmas under hydrous conditions amphibole is the dominant crystallizing ferromagnesian phase and subsequently will remove Y from the melt, thus increasing the Hf/Y values (Moore and Carmichael, 1998; Gagnevin et al. 2010; Richards et al., 2012; Loucks, 2014; Large et al. 2018).

The early, Guichon Creek rocks have higher Hf/Y ratios (5-60) and Th/U (0.4-1) compared to later more felsic melts. As the melts evolved into higher felsic composition, lesser

amounts of amphibole crystallized and increased amounts of both apatite and titanite crystallized. This crystallizing assemblage reduces the Hf/Y ratio, as observed in the Bethlehem rocks and dikes (6-50) and late intrusive rocks (8-35). The younger Guichon Creek rocks, in addition, show an increase in apatite and titanite as accessory phases (D'Angelo et al. 2017). The late "S&P" Bethsaida and QFPQ dikes primarily have low Hf/Y values (1-50), but also have a few elevated values similar to the early Guichon Creek rocks. The locally elevated Hf/Y values in zircon crystals from the late dikes resulted from the mixing of the evolved upper crustal melt (low Y and high Hf) with a more mafic melt (with higher Y content; Fig. 8). The change in texture (finer-grained granular) despite similar whole rock composition (Fig. 4) between the "S&P" Bethsaida and the Bethsaida facies could reflect the thermal influx of this new melt.

The Gump Lake stock zircons have trace element compositions (Fig. 9) as well as elevated Yb/Gd_N (Fig. 10A, B) and low Hf/Y (Fig. 10C) ratios similar to the younger facies of the Guichon Creek batholith. These zircon compositions suggest the Gump Lake stock was more evolved relative to the early Guichon Creek batholith facies, consistent with the more felsic composition of the stock (Fig. 4). However, the low Eu/Eu* and Ce/Ce* values (Fig. 11) suggest the melt formed under late-stage feldspar fractionating conditions (Ballard et al. 2001; Dilles et al. 2015; Lee et al. 2017b). The increase of zircon Eu/Eu* values with temporal evolution despite the compositional differences between the Gump Lake stock and the Guichon Creek facies is potentially due to an increase in fluid content from fractional crystallization in a lower or mid-crustal source, and that subsequent intrusion into the upper crust over time likely primed the host rocks for economic mineralization (Fig. 12; Rohrlach and Loucks, 2005; Lee et al. 2017a). Therefore, identifying igneous suites that show this variation is key to determining the potential fertility of the region.

Whole rock trace element compositions of the middle to late Guichon Creek batholith facies have high La/Yb, Sr/Y, and V/Sc ratios that increase with decreasing age (D'Angelo et al. 2017), and these changes are interpreted to be the result of fractional crystallization of amphibole from hydrous and oxidized magmas (Lang and Titley 1998; Richards et al. 2001; Rorlach and Loucks, 2005; Richards et al. 2012; Loucks 2014; Wang et al. 2014; D'Angelo et al. 2017; Hou and Wang, 2019). The trace element composition of zircon from the Guichon Creek batholith are consistent with crystallization from at least five pulses of hydrous and oxidized magmas, and also record the change in the fractional crystallization of the source magma(s) with time (Table 2). Whole rock and zircon compositions of the Gump Lake stock (Fig. 4) suggest an earlier, relatively smaller, evolved melt intruded into the Nicola Group before the formation of the mafic melts of the Border facies.

Europium and cerium content of zircon as an indicator of oxidation state and potential magma fertility

Europium and Ce anomalies in zircon have been proposed to reflect oxidizing conditions or water content in magmas that host, or form, ore deposits (Ballard et al. 2002; Chelle-Michou et al. 2014; Shen et al. 2015; Lu et al. 2016). Under normal fractional crystallization, Eu/Eu_N^* values in zircon will decrease rapidly as Eu is removed from the melt by plagioclase crystallization, resulting in larger negative Eu anomalies in zircon with time (low Eu/Eu_N^* values; Streck and Dilles 1998; Chamberfort et al. 2008; Dilles et al. 2015; Lee et al. 2017b). Dilles et al. (2015) argued that anomalously high (>0.4) Eu/Eu_N^* is due to SO_2 degassing in the melt, and that an increase in fluid content in the melt suppresses plagioclase crystallization and subsequent removal of Eu^{2+} in the crystallizing melt. It has also been suggested that fractional crystallization of titanite and apatite during zircon growth is the cause of Eu/Eu* variation in the

zircon crystals (e.g., Loader et al. 2017; Rezeau et al. 2019). The Eu/Eu* and Ce/Ce* values of the Guichon Creek batholith are similar to values reported from other mineralized porphyry magmatic suites, and these ratios change with each successive intrusion (Fig. 11).

Zircon crystals from the early Border and Highland Valley facies generally have low (<0.4) Eu/Eu_N* values, although there is overlap with the younger facies (Fig. 6). Zircon in the Guichon subfacies has the lowest Eu/Eu_N* values (≤0.34), whereas zircon from the slightly younger Chataway subfacies has Eu/Eu_N* ranging from 0.32 to 0.72 (ESM Table S4). The high values in the Chataway sample are all from rim analyses, suggesting that the change in Eu/Eu_N* composition occurred late and at relatively low temperature during the crystallization of the zircon. Furthermore, the Eu/Eu_N* values increase with increasing Hf content in zircon rims (Fig. 6B) implying that the elevated Eu/Eu_N* in the zircon from the Chataway sample occurred late in the crystallization of the melt (Claiborne et al. 2006; Watson et al. 2006; Wooden et al. 2006; Dilles et al. 2015; Lee et al. 2017b). There are two possible reasons for the higher Eu/Eu_N* values in the younger sample: (1) increasing water content in the melt as a result of evolution through the crystallization of the Highland Valley magma; or (2) mixing of pre-existing magma in a shallow chamber with a later pulse of magma with elevated Eu^{3+} concentrations. The first explanation is the more likely one, as the Highland Valley facies evolve from higher to lower volumes of Fe-bearing minerals and to lower whole rock Fe-content as well to more hydrous and oxidizing conditions from the Guichon to the Chataway sub-facies (Fig. 4; Byrne et al. 2013; D'Angelo et al. 2017).

Figure 12 shows the distribution of zircon Eu/Eu_N* values over time for the Guichon Creek batholith. The overall increase in Eu/Eu_N* values through time and the sharp decrease coincident with the deposition of sulfide mineralization suggests that the zircon trace element

composition does have the potential for use as a proxy for porphyry copper potential. Although several arguments have been presented as to the cause of Eu anomalies in zircon, these values can be used to track the evolution of the crystallizing magma chamber, and elevated Eu anomalies have been observed in multiple porphyry copper deposits (Liang et al. 2006; Wainwright et al. 2011; Wang et al. 2013; Dilles et al. 2015; Shen et al. 2015; Lu et al. 2016; Banik et al. 2017; Lee et al. 2017b; Large et al. 2018; Bouzari and Hart, 2019).

The Ce concentration in zircon commonly increases when increased oxygen fugacity converts some Ce^{3+} to Ce^{4+}; the latter preferentially partitions into the Zr^{4+} site (Ballard et al. 2002; Trail et al. 2012). The Ballard et al. (2002) method of calculating Ce^{4+}/Ce^{3+} requires accurate whole-rock Ce concentration and significant assumptions about the partitioning of REE between the zircon and crystallizing melt (Trail et al. 2012; Dilles et al. 2015). Calculation of the cerium anomaly using values of La and Pr is problematic as determined by the LA-ICP-MS method due to the detection limits of these elements. The method of Loader et al. (2017), which uses the concentration of Nd and Sm to determine Ce/Ce_N^* has been suggested as a proxy for Ce^{4+}/Ce^{3+} values. However, the method calculates the expected Ce value along a straight line, which can overestimate the Ce_N^*value due to the concave nature of REE. Zhong et al. (2019) propose using a curve fit line function based on the MREE and HREE zircon values to calculate the Ce* value. This method avoids the uncertainty of La and Pr due to analytical measurement and depending on the line curve fit (r^2) a potentially robust value for Ce*. Comparing the Ce/Ce* and Eu/Eu* values using both methods (ESM Figure S2), the Ce/Ce_C^*values are several orders of magnitude higher compared to the Ce/Ce_N^* reflecting the overestimation of Ce* using the method of Loader et al. (2019). While the Ce/Ce_C^* method represents a probable more representative estimation of Ce*, the calculation of Eu/Eu_C^* is problematic as despite the strong

fit of the curves (r^2 values > 0.96; ESM Table S5) the MREE (Sm, Eu, and Gd) values are lower than the analytical values. Thus, we prefer to use the traditional Eu/Eu_N^* method as it is based on analytically derived data.

The zircon Ce/Ce_C^* values for the early to middle Guichon Creek rocks generally range from ~40 to ~1700, although one sample from the Gump Lake stock yielded a value of 5200 and two values from the early Guichon Creek rocks were over 3000 (Fig. 11). The late Guichon Creek rocks range from 35 to over 6000, with the majority of the data for the main Guichon Creek rocks increasing in Ce/Ce_C^* with increasing Eu/Eu_C^* values, consistent with an elevated oxidation state (Zhong et al. 2019). The ”S&P” Bethsaida and the QFPQ dike have high Ce concentrations relative to the other Guichon Creek batholith facies (Figs. 9A, 9B), with the highest calculated Ce/Ce_C^*, and lower Eu/Eu_N^* values compared to the main intrusive facies (Fig. 11). The high Ce/Ce_C^* values in the late ”S&P” Bethsaida and QFPQ dike cannot be explained by the oxidation state alone as the low (<0.30) Eu/Eu_N^* values suggest a lower oxidation state of the source melt or a relatively dry melt that fractionated feldspar. Additionally, the whole rock compositions of both dikes have low total REE contents, low Fe/S and Zr/Hf values, and distinct negative Eu anomalies suggesting that feldspar was a main crystallizing phase during the formation of these rocks (Fig. 4C, ESM Table S2). These values, along with the aplitic nature of these rocks and high feldspar content (D’Angelo et al. 2017), could be attributed to late crystallization through filter pressing (Sisson and Bacon 1999; Bachmann and Bergantz, 2006). The elevated Ce/Ce_C^* values in the ”S&P” Bethsaida and QFPQ dike zircon are consistent with zircon that formed from volatile-rich, crystal poor magmas (i.e., Erdmann et al. 2013). Alternatively, an influx of a new, higher temperature melt in which titanite and zircon had not crystallized, could have enriched the zircon in Ce, as well as other trace elements.

Zircon composition as a proxy for mineralization event

Calculated temperatures are consistent with the results of other studies of silicic intrusions and volcanic rocks using similar methods (e.g., Claiborne et al. 2010; Dilles et al. 2015; Lee et al. 2017b; Loader et al. 2017). Most rock facies in the Guichon Creek batholith show a general decrease in Ti-in-zircon temperature with increasing Hf content that is consistent with crystallization from a melt in a cooling upper magma chamber (Fig. 7). The "S&P" Bethsaida is an exception as it trends to higher temperatures with increasing Hf concentrations (Fig. 7D). The positive correlation between Ti, Hf, and the enriched chemical signature could reflect the influx of a higher temperature magma (up to 800 °C), into the upper crustal magma chamber (Lee et al. 2017b; Large et al. 2018). Additionally, this late melt is enriched in Y, REE, Nb, and Ta relative to the Bethsaida magma as the zircons from the syn- to post-mineral dikes have elevated abundances of these elements (Figs. 8-10). Increased oxidation of the melt at volatile saturation will increase the REE, Nb, and Ta composition in zircon as this affects the zircon-melt partitioning (Bacon et al. 2007; Van Lichtervelde et al. 2011; Erdmann et al. 2013). The heat or volatiles released from this event increased the temperatures recorded in the zircons from the "S&P" Bethsaida (Fig. 7D) and may have triggered the mineralization event at the Valley-Lornex-Highmont deposit. The timing of this event was closely related to the release of a Cu-bearing magmatic volatile phase because the "S&P" Bethsaida is mineralized, whereas the QFPQ (which has similar zircon compositions) is weakly to un-mineralized (Byrne et al. 2013; D'Angelo et al. 2017). The QFPQ is ~one million years younger than the "S&P" Bethsaida, and while we have compared the composition of the two rock types and zircon together, the texture, elevated trace element composition, and age difference would suggest that the younger dike most likely formed as the last batch of crystal-poor intrusion from the crystallizing Guichon Creek

569 batholith. The textural oscillatory growth zoning (Fig. 3L), as well as the trace element
570 composition in the QFPQ zircon, are consistent with this suggestion (Bacon et al. 2007; Erdmann
571 et al. 2013).

572 We hypothesize that the input of fresh melt into the Bethsaida magma triggered the
573 release of water, Cl and SO_2 from a hydrous (>5 wt. %) partially crystallized melt and that this
574 fluid produced the large Valley-Lornex-Highmont deposits. A more primitive, deep-sourced
575 magmatic flux as a trigger for the formation of the smaller Bethlehem deposit is not evident from
576 the Bethlehem porphyry zircons, but the decreasing Eu/Eu_N^* with increasing Hf (Fig. 6D)
577 implies fractional crystallization was ongoing under elevated oxidation conditions within the
578 crystallizing magma chamber.

579 **Sequence of events in the Guichon Creek batholith leading to porphyry Cu formation**

580 The zircon trace element composition generally supports the model of formation for the
581 Guichon Creek batholith proposed by D'Angelo et al. (2017), where partial melts derived from
582 the asthenosphere fractionated in a deep crustal magma chamber, increasing fluid content and
583 ascended in two to three pulses into a mid- to upper crustal chamber. However, results from this
584 study suggest the cyclical emplacement of five magmatic pulses (Table 2) that were emplaced
585 into an upper magma chamber from the lower crust (Fig. 13). The new CA-TIMS age for the
586 Gump Lake stock extends intrusive magmatism for the region to at least 11 Ma, with initial
587 magmatism occurring at 218.01 ± 0.18 Ma and culminating with the QFPQ dike at 206.95 ± 0.22
588 Ma (ESM Table S1). The zircons from the Gump Lake stock crystallized from a low-temperature
589 (<750 °C; Fig. 7A) evolved (high Yb/Gd_N, low Hf/Y and Eu/Eu_N values; Fig. 10) felsic melt.
590 The Gump Lake stock was derived from the initial melting of the subarc mantle during

591 subduction of the Quesnel terrane, which then ascended into the crust. Continued evolution
592 through plagioclase crystallization formed the Gump Lake melt, which intruded into the
593 overlying Nicola Group. Emplacement likely occurred along pre-existing structural corridors that
594 weakened the crust and were subsequently the pathways for the emplacement of the Guichon
595 Creek batholith (Lesage et al., 2019).

596 Following the emplacement of the Gump Lake stock, a second pulse of melt from the
597 lower crust that had undergone assimilation-fractional crystallization rose to form the initial
598 upper crustal chamber for the gabbros, diorites, and granodiorites of the Border facies, which
599 assimilated the early Triassic Nicola Group volcanic rocks. Continued melt input through time
600 inflated this upper chamber, and subsequent inward crystallization formed the two subfacies
601 (Guichon and Chataway) of the Highland Valley facies. The continued evolution of lower- to
602 mid-crustal magma chambers elevated the water content of the third magmatic pulse which was
603 then emplaced into the upper chamber, and a partially crystalized Chataway subfacies, as the
604 Bethlehem granodiorite. The contact between the Highland Valley facies and the Bethlehem
605 facies varies from gradational to sharp, and the Bethlehem facies is interpreted to have been
606 emplaced before the complete solidification of the Highland Valley facies (Byrne et al. 2013;
607 D'Angelo et al. 2017). The Bethlehem melt, as well as a copper-bearing magmatic volatile
608 phase, is inferred to have been concentrated in the cupola of the batholith and was the source for
609 genetically related porphyry dikes, stocks, and fluids that caused brecciation and mineralization
610 at the Bethlehem porphyry occurrence. The complex Eu/Eu_N^* values in the syn- to post-mineral
611 Bethlehem dikes (Fig. 6D) highlight the increasing fluid content and subsequent fluid release
612 during mineralization at ~208 Ma (Byrne et al. 2013).

A fourth, oxidized, magmatic pulse intruded the Bethlehem facies, cross-cut earlier mineralization, and formed the Skeena and Bethsaida granodiorites. The zircon compositional trends in the late ”S&P” Bethsaida suggest that a final fifth pulse of higher temperature, possibly less oxidized (i.e., low Eu/Eu_N* values), intruded into the main magma chamber. We suggest that this fifth magmatic event triggered the release of magmatic volatile phases (H_2O, Cl, and SO_2), metal scavenging, and promoted highly oxidizing conditions throughout the fourth pulse of partially crystallized magma. Subsequent metal-bearing fluids were focused in a cupola region and porphyry dike complexes located in the center of the batholith and subjacent Valley-Lornex-Highmont porphyry Cu system. Continued crystallization of this volatile-magma through filter pressing formed the final post-mineral QFPQ as well as the porphyritic and aplitic dikes in the region and enriched the zircon in Y, REE, Nb, and Ta.

The long-lived history of magmatism in the region, as well as evidence for multiple pulses of magmatism, increased the mineralizing potential (fractional crystallization, magma mixing, crustal assimilation: Grunder et al. 2008; Memeti et al. 2010) of the magma chamber from which porphyry Cu-(Mo) mineralization is derived (Rohrlach and Loucks, 2005; Richards et al. 2012; D’Angelo et al. 2017). Zircon compositions from the Guichon Creek intrusive suite record this complex history through changes in oxidation state, temperature, and trace element content. The evolution of the Guichon Creek batholith is similar to some other fertile plutonic-arc districts in which prolonged magmatism, coupled with a late-stage magmatic flux, formed the large tonnage porphyry deposit (Richards et al. 2012). The complex cyclical magma emplacement, mixing, cooling and degassing evident in the Guichon Creek batholith is consistent with observations from other porphyry systems (Cooke et al. 2005; Hollings et al. 2011; Chambefort et al. 2013).

Conclusions

Zircon trace element content collected via the LA-ICP-MS method from the Guichon Creek batholith provides a detailed thermal and compositional magmatic history and potential for ore fertility that is not apparent from whole-rock chemistry alone. The presence of high Eu/Eu_N^* values with elevated Hf concentration is a reliable indicator of elevated water content and potential fertility, as suggested by Dilles et al. 2015 and Lee et al. 2017b. Zircon from the 218 ± 0.18 Ma Gump Lake stock has Eu/Eu_N^* values <0.40, as well as lower zircon temperature range and higher trace element concentration (Y, Nb, Ta, Yb), compared to the early Guichon Creek intrusions and represents the initial pulse of magmatism in the region. The magmatic rocks that make up the initial formation of the Guichon Creek batholith (211.0-210.5 Ma) have Eu/Eu_N^* values less than 0.45 except for the Chataway sub-facies, which range from 0.32 to 0.72. Calculated zircon temperatures for the early Guichon Creek rocks have a higher range compared to the younger intrusions, and the trace element content is lower in zircon from the older rocks. The intrusion of these more mafic magmas formed the early magma chamber, which evolved to form volatile-rich magmas of the Chataway sub-facies and younger magmatic pulses through fractional crystallization of amphibole, apatite, and titanite. The anomalous Eu/Eu_N^* values observed in zircon from the middle and late intrusions are the result of increased oxidation state, which primed the batholith for mineralization. The mid- to late- Guichon Creek batholith rocks, which range in age from ~209.5 to 207 Ma and host the primary Cu deposits of the Highland Valley Copper district, have higher Eu/Eu_N^*. The late dikes of the possible fifth magmatic pulse have a large range of Eu/Eu_N^* values down to 0.19, high Ce/Ce_C^* values, and high concentrations of REE as well as Y, Nb, and Ta that is interpreted to reflect an influx of mafic(?) melt from the lower to mid-crust and ongoing crystallization of the silicic melt. The fluid that

659 was subsequently released following the intrusion and mixing of the late magmas related to the
660 syn-mineral “S&P” Bethsaida formed the porphyry Cu deposits at Valley-Lornex and Highmont
661 at ~208-207 Ma.

662 **Acknowledgments**

663 The authors thank Teck Resources Limited for providing access to the samples used in
664 this study as well as the logistical assistance for all the project work. In particular, we thank
665 Andrew Davies, Lucas Marshall, James Stemler, Gerald Grubisa, John Ryan, Suzanne Byron,
666 and Semyon Martynenko. We also thank Marghaleray Amini for help with the LA-ICP-MS
667 analyses at the Pacific Centre for Isotopic and Geochemical Research. Early discussions with
668 John H. Dilles helped define the scope of this project, and reviews by Dilles, Yongjun Lu, Rui
669 Wang, and Jeremy Richards have helped us improve the manuscript. The authors also thank Rui
670 Wang, Ilkay Kuşcu, and associate editor David Banks and editor Georges Beaudoin for their
671 extensive review of this manuscript. All funding for this project was provided through the
672 Natural Sciences and Engineering Research Council of Canada (NSERC) and the Canadian
673 Mining Innovation Council (CMIC) Mineral Exploration Footprints project. This manuscript is
674 NSERC-CMIC Mineral Exploration Footprints Project contribution number 168 and MDRU
675 publication number 405.

676 **References**

677 Ager CA, Ulrych TJ, McMillan WJ (1973) A Gravity Model for the Guichon Creek Batholith,
678 South-central British Columbia. Can J Earth Sci 10:920–935

679 Aiuppa A, Baker DR, Webster JD (2009) Halogens in volcanic systems. Chem Geol 263:1–18

680 Anders E, Grevesse N (1989) Abundance of the elements. Geochim Cosmochim Acta 53:197–
681 214

682 Ash CH, Reynolds PH, Creaser RA, et al (2007) $^{40}Ar/^{39}Ar$ and Re-O Isotopic Ages for
683 Hydrothermal Alteration and Related Mineralization at the Highland Valley Cu-Mo Deposit
684 (NTS 092I), Southwestern British Columbia. Geol Fieldwork 2006, Br Columbia Geol
685 Surv Pap 2007-1 19–24

686 Bachmann O, Bergantz GW (2006) Gas percolation in upper-crustal silicic crystal mushes as a
687 mechanism for upward heat advection and rejuvenation of near-solidus magma bodies. J
688 Volcanol Geotherm Res 149:85–102

689 Bacon CR, Sisson TW, Mazdab FK (2007) Young cumulate complex beneath Veniaminof
690 caldera, Aleutian arc, dated by zircon in erupted plutonic blocks. Geology 35:491–494

691 Baker DR, Conte AM, Freda C, Ottolini L (2002) The effect of halogens on Zr diffusion and
692 zircon dissolution in hydrous metaluminous granitic melts. Contrib to Mineral Petrol
693 142:666–678

694 Ballard JR, Palin JM, Campbell IH (2002) Relative oxidation states of magmas inferred from
695 Ce“IV”/Ce“III” in zircon: Application to porphyry copper deposits of northern Chile.
696 Contrib to Mineral Petrol 144:347–364

697 Banik TJ, Coble MA, Miller CF (2017) Porphyry Cu formation in the middle Jurassic Yerington
698 batholith, Nevada, USA: Constraints from laser Raman, trace element, U-Pb age, and
699 oxygen isotope analyses of zircon. Geosphere 13:GES01351.1. doi: 10.1130/GES01351.1

700 Bissig T, Leal-mejía H, Stevens RB, Hart CJR (2017) High Sr/Y Magma Petrogenesis and the
701 Link to Porphyry Mineralization as Revealed by Garnet-Bearing I-Type Granodiorite
702 Porphyries of the. Econ Geol 112:551–568

703 Black LP, Kamo SL, Allen CM, et al (2003) TEMORA 1: A new zircon standard for
704 Phanerozoic U-Pb geochronology. Chem Geol 200:155–170

705 Bouzari F, Hart CJR (2019) Assessing British Columbia Porphyry Fertility Using Zircons.
706 Geosci BC Summ Act 2018 Miner Mining, Geosci BC, Rep 2019–1:45–54

707 Bouzari F, Hart CJR, Bissig T, Barker S (2016) Hydrothermal alteration revealed by apatite
708 luminescence and chemistry: A potential indicator mineral for exploring covered porphyry
709 copper deposits. Econ Geol 111:1397–1410. doi: 10.2113/econgeo.111.6.1397

710 Burnham AD, Berry AJ, Halse HR, et al (2015) The oxidation state of Eu in silicate melts as a
711 function of oxygen fugacity, composition and temperature. Chem Geol 411:248–259

712 Byrne K, Lesage G, Gleeson SA, Lee RG (2017) Large-Scale Sodic-Calcic Alteration Around
713 Porphyry Copper Systems: Examples from the Highland Valley Copper District, Guichon
714 Batholith, South-Central British Columbia. Geosci BC Summ Act 2016 213–222

715 Byrne K, Stock E, Ryan J, et al (2013) Porphyry Cu-(Mo) deposits in the Highland Valley
716 district, south-central British Columbia. Soc Econ Geol F Trip Guideb 43:99–116

717 Candela PA (1992) Controls on ore metal ratios in granite-related ore systems: An experimental
718 and computational approach. Trans R Soc Edinburgh, Earth Sci 83:317–326

719 Casselman MJ, McMillan WJ, Newman KM (1995) Highland Valley porphyry copper deposits
720 near Kamloops, British Columbia: A review and update with emphasis on the Valley
721 deposit. In: Schroeter TG (ed) Porphyry deposits of the Northwestern Cordillera of North
722 America: Canadian Institute of Mining and Metallurgy, Special Volume 46. pp 161–191

723 Chambefort I, Dilles JH, Kent AJR (2008) Anhydrite-bearing andesite and dacite as a source for
724 sulfur in magmatic-hydrothermal mineral deposits. Geology 36:719–722

725 Chambefort I, Dilles JH, Longo AA (2013) Amphibole geochemistry of the Yanacocha
726 Volcanics, Peru: Evidence for diverse sources of magmatic volatiles related to gold ores. J
727 Petrol 54:1017–1046

728 Clairborne LL, Miller CF, Walker BA, et al (2006) Tracking magmatic processes through Zr/Hf
729 ratios in rocks and Hf and Ti zoning in zircons: An example from the Spirit Mountain
730 batholith, Nevada batholith, Nevada. Mineral Mag 70:571–543

731 Clairborne LL, Miller CF, Wooden JL (2010) Trace element composition of igneous zircon: a
732 thermal and compositional record of the accumulation and evolution of a large silicic
733 batholith, Spirit Mountain, Nevada. Contrib to Mineral Petrol 160:511–531

734 Cline JS, Bodnar RJ (1991) Can economic porphyry copper mineralization be generated by a
735 typical calc-alkaline melt? J Geophys Res 96:8113–8126

736 Colombini LL, Miller CFM, Gualda GAR, et al (2011) Sphene and zircon in the Highland Range
737 volcanic sequence (Miocene, southern Nevada, USA): elemental partitioning, phase
738 relations, and influence on evolution of silicic magma. Mineral Petrol 102:29–50

739 Cooke DR, Hollings P, Walshe JL (2005) Giant porphyry deposits: Characteristics, distribution,
740 and tectonic controls. Econ Geol 100:801–818

741 Crowley JL, Schoene B, Bowring SA (2007) U-Pb dating of zircon in the Bishop Tuff at the
742 millennial scale. Geology 35:1123–1126

743 D'Angelo M, Alfaro M, Hollings P, et al (2017) Petrogenesis and magmatic evolution the
744 Guichon Creek Batholith: Implications for the Highland Valley porphyry Cu ± (Mo)
745 district, southcentral British Columbia. Econ Geol 112:1857–1888

746 D'Angelo M (2016) Geochemistry, petrography and mineral chemistry of the Guichon Creek
747 and Nicola batholiths, southcentral British Columbia. unpublished MSc. thesis, Lakehead
748 University, Thunder Bay, Ontario

749 Dilles JH (1987) The petrology of the Yerington batholith, Nevada: Evidence for the evolution
750 of porphyry copper ore fluids. Econ Geol 82:1750–1789

751 Dilles JH, Kent AJR, Wooden JL, et al (2015) Zircon compositional evidence for sulfur-
752 degassing from ore-forming arc magmas. Econ Geol 110:241–251

753 Djouka-Fonkwe ML, Kyser K, Clark AH, et al (2012) Recognizing propylitic alteration
754 associated with porphyry Cu-Mo deposits in lower greenschist facies metamorphic terrain
755 of the Collahuasi district, northern chile-implications of petrographic and carbon isotope
756 relationships. Econ Geol 107:1457–1478

757 Ferry JM, Watson EB (2007) New thermodynamic models and revised calibrations for the Ti-in-
758 zircon and Zr-in-rutile thermometers. Contrib to Mineral Petrol 154:429–437

759 Field CW, Zhang L, Dilles JH, et al (2005) Sulfur and oxygen isotopic record in sulfate and
760 sulfide minerals of early, deep, pre-Main Stage porphyry Cu-Mo and late Main Stage base-
761 metal mineral deposits, Butte district, Montana. Chem Geol 215:61–93

762 Gagnevin D, Daly JS, Kronz A (2010) Zircon texture and chemical composition as a guide to
763 magmatic processes and mixing in a granitic environment and coeval volcanic system.
764 Contrib to Mineral Petrol 159:579–596. doi: 10.1007/s00410-009-0443-0

765 Grunder AG, Klemetti EW, Feeley TC, McKee CM (2008) Eleven million years of arc
766 volcanism at the Aucanquilcha volcanic cluster, northern Chilean Andes: Implications for
767 the life span and emplacement of plutons. Trans R Soc Edinburgh 97:415–436

768 Hanchar JM, van Westrenen W (2007) Rare earth element behavior in zircon-melt systems.
769 Elements 3:37–42

770 Hanchar JM, Watson EB (2003) Structure and chemistry of zircon and zircon-group minerals.
771 Rev Mineral Geochemistry 53:89–112

772 Hayden LA, Watson EB (2007) Rutile saturation in hydrous siliceous melts and its bearing on
773 Ti-thermometry of quartz and zircon. Earth Planet Sci Lett 258:561–568. doi:
774 10.1016/j.epsl.2007.04.020

775 Hollings P, Cooke DR, Waters PJ, Cousens B (2011) Igneous geochemistry of mineralized rocks
776 of the Baguio district, Philippines: Implications for tectonic evolution and the genesis of
777 porphyry-style mineralization. Econ Geol 106:

778 Hou Z, Wang R (2019) Fingerprinting metal transfer from mantle. Nat Commun 10:9–11. doi:
779 10.1038/s41467-019-11445-w

780 Lang JR, Titley SR (1998) Isotopic and geochemical characteristics of Laramide magmatic
781 systems in Arizona and implications for the genesis of porphyry copper deposits. Econ Geol
782 93:138–170

783 Large SJE, von Quadt A, Wotzlaw J-F, et al (2018) Magma evolution leading to porphyry Au-Cu
784 mineralization at the Ok Tedi deposit, Papua New Guinea: trace element geochemistry and
785 high-precision geochronology of igneous zircon. Econ Geol 113:39–61

786 Lee RG, Byrne K, Alfaro M, et al (2017a) Assessing the zircon compositional evolution from the
787 Guichon Creek Batholith and Highland Valley Copper. Proc 14th Bienn SGA Meet 20-23
788 August 2017, Quebec City, Canada 3:1087–1090

789 Lee RG, Dilles JH, Tosdal RM, et al (2017b) Magmatic evolution of granodiorite intrusions at
790 the El Salvador porphyry copper deposit, Chile, based on trace element composition and
791 U/Pb age of zircons. Econ Geol 112:245–273

792 Lesage G, Byrne K, Lypaczewski P, et al (2016) Characterizing the district-scale alteration
793 surrounding a large porphyry Cu system: The footprint of Highland Valley Copper, British
794 Columbia. GAC-MAC Abstr June 1-3, 2016, Whitehorse, CA, 39:52

795 Lesage G, Byrne K, Morris WA, et al (2019) Interpreting regional 3D fault networks from
796 integrated geological and geophysical data sets: An example from the Guichon Creek
797 batholith, British Columbia. J Struct Geol 119:93–106. doi: 10.1016/j.jsg.2018.12.007

798 Liang HY, Campbell IH, Allen C, et al (2006) Zircon Ce^{4+}/Ce^{3+} ratios and ages for Yulong ore-
799 bearing porphyries in eastern Tibet. Miner Depos 41:152–159

800 Loader MA, Wilkinson JJ, Armstrong RN (2017) The effect of titanite crystallisation on Eu and
801 Ce anomalies in zircon and its implications for the assessment of porphyry Cu deposit
802 fertility. Earth Planet Sci Lett 472:107–119

803 Logan JM, Mihalynuk MG (2014) Tectonic controls on early Mesozoic paired alkaline porphyry
804 deposit belts (Cu- Au±Ag-Pt-Pd-Mo) within the Canadian Cordillera. Econ Geol 109:827–
805 858

806 Loucks RR (2014) Distinctive composition of copper-ore-forming arc magmas. Aust J Earth Sci
807 61:5–16

808 Lu Y, Loucks RR, Fiorentini M, et al (2016) Zircon Compositions as a Pathfinder for Porphyry
809 Cu ± Mo ± Au Deposits. Econ Geol Spec Publ 19:329–347

810 Massey NWD, MacIntyre DG, Desjardins PJ, Cooney RT (2005) Digital Geology Map of British
811 Columbia. BC Minist Energy Mines, Whole Prov Geofile 2005-1

812 Mattinson JM (2005) Zircon U-Pb chemical abrasion ("CA-TIMS") method: Combined
813 annealing and multi-step partial dissolution analysis for improved precision and accuracy of
814 zircon ages. Chem Geol 220:47–66

815 Mazdab FK, Wooden JL (2006) Trace element analysis in zircon by ion microprobe (SHRIMP-
816 RG): Technique and applications. Geochim Cosmochim Acta Suppl 70:405

McDonough WF, Sun S (1995) The composition of the Earth. Chem Geol 120:223–253

McMillan WJ (1976) Geology and Genesis of the Highland Valley Ore Deposits and the Guichon Creek Batholith. In: Sutherland Brown A (ed) Porphyry Deposits of the Canadian Cordillera: Canadian Institute of Mining and Metallurgy. pp 85–104

McMillan WJ (1985) Geology and ore deposits of the Highland Valley Camp. In: Sinclair AJ (ed) Mineral Deposits Division Field Guide and Reference Manual Series, no. 1: Geological Association of Canada. p 121

McMillan WJ, Anderson RG, Chen R, Chow W (2009) Geology and mineral occurrences (MINFILE), the Guichon Creek Batholith and Highland Valley porphyry copper district, British Columbia: Geological Survey of Canada, Open file 6079, 2 sheets

Memeti V, Paterson S, Matzel J, et al (2010) Magmatic lobes as “snapshots” of magma chamber growth and evolution in large, composite batholiths: An example from the Tuolumne intrusion, Sierra Nevada, California. Bull Geol Soc Am 122:1912–1931

Mihalynuk MG, Diakow LJ, Friedman RM, Logan JM (2016) Chronology of southern Nicola arc stratigraphy and deformation. Br Columbia Geol Surv Geol Fieldwork 2015, Pap 2016-1 31–63

Miller CF, McDowell SM, Mapes RW (2003) Hot and cold granites? Implications of zircon saturation temperatures and preservation of inheritance. Geology 31:529–532

Moore CM, Carmichael ISE (1998) The hydrous phase equilibria (to 3 kbar) of an andesite and basaltic andesite from western Mexico: Constraints on water content and conditions of phenocryst growth. Contrib to Mineral Petrol 130:304–319

Mortimer N (1987) The Nicola Group: Late Triassic and Early Jurassic subduction-related volcanism in British Columbia. Can J Earth Sci 24:2521–2536

Mortimer N (1986) Late Triassic, arc-related, potassic igneous rocks in the North American Cordillera. Geology 14:1035–1038

Mundil R, Ludwig KR, Metcalfe I, Renne PR (2004) Age and timing of the Permian mass extinctions: U/Pb dating of closed-system zircons. Science 305:117–123

Northcote KE (1969) Geology and Geochronology of the Guichon Creek Batholith. Bull 56, Br Columbia Dep Mines Pet Resour 77

Olson NH, Dilles JH, Kent AJR, Lang JR (2017) Geochemistry of the Cretaceous Kaskanak Batholith and genesis of the Pebble porphyry Cu-Au-Mo deposit, Southwest Alaska. Am Mineral 102:1597–1621

Paton C, Hellstrom J, Paul B, et al (2011) Iolite: Freeware for the visualization and processing of mass spectrometric data. J Anal At Spectrom 26:2508–2518

Piccoli P, Candela P, Rivers M (2000) Interpreting magmatic processes from accessory phases: titanite—a small-scale recorder of large-scale processes. Trans R Soc Edinb Earth Sci 91:257–267. doi: 10.1017/S0263593300007422

Preto VA (1979) Geology of the Nicola Group between Merritt and Princeton. Br Columbia Minist Energy, Mines Pet Resour Bull 69 85

Ray GE, Dawson GL, Webster ICL (1996) The stratigraphy of the Nicola group in the Hedley district, British Columbia, and the chemistry of its intrusions and Au skarns. Can J Earth Sci 33:1105–1126

Rezeau H, Moritz R, Wotzlaw J-F, et al (2019) Zircon petrochronology in the ore-bearing Meghri-Ordubad pluton, Lesser Caucasus: fingerprinting igneous processes with implications for the exploration of porphyry Cu-Mo deposits. Econ Geol 114:1365–1388Richards JP (2003) Tectono-magmatic precursors for porphyry Cu-(Mo-Au) deposit formation. Econ Geol 98:1515–1533

Richards JP (2015) The oxidation state, and sulfur and Cu contents of arc magmas: implications for metallogeny. Lithos 233:27–45

Richards JP, Spell T, Rameh E, et al (2012) High Sr/Y magmas reflect arc maturity, high magmatic water content, and porphyry Cu ± Mo ± Au potential: Examples from the Tethyan arcs of central and eastern Iran and Western Pakistan. Econ Geol 107:295–332

Rohrlach BD, Loucks RR (2005) Multi-million-year cyclic ramp-up of volatiles in a lower crustal magma reservoir trapped below the Tampakan Cu-Au deposit by Mio-Pliocene crustal compression in the southern Philippines. In: Porter TM (ed) Super porphyry copper and gold deposits, Australia, PCG Publishing,v. 2. pp 369–407

Roy B, Clowes RM (2000) Seismic and potential-field imaging of the Guichon Creek batholith, British Columbia, Canada, to delineate structures hosting porphyry copper deposits. Geophysics 65:1418–1434

Schmitz MD, Schoene B (2007) Derivation of isotope ratios, errors, and error correlations for U-Pb geochronology using 205Pb-235U-(233U)-spiked isotope dilution thermal ionization mass spectrometric data. Geochemistry Geophys Geosystems 8:Q08006

Scoates JS, Friedman RM (2008) Precise age of the platiniferous Merensky Reef, Bushveld Complex, South Africa, by the U-Pb ID-TIMS chemical abrasion ID-TIMS technique. Econ Geol 103:465–471

Sha L-K, Chappell BW (1999) Apatite chemical composition, determined by electron microprobe and laser-ablation inductively coupled plasma mass spectrometry, as a probe into granite petrogenesis. Geochim Cosmochim Acta 63:3861–3881

Shen P, Hattori K, Pan H, et al (2015) Oxidation condition and metal fertility of granitic magmas: Zircon trace-element data from porphyry Cu deposits in the central Asian orogenic belt. Econ Geol 110:1861–1878

Sisson TW, Bacon CR (1999) Gas-driven filter pressing in magmas. Geology 27:613–616

Sláma J, Košler J, Condon DJ, et al (2008) Plešovice zircon - A new natural reference material for U-Pb and Hf isotopic microanalysis. Chem Geol 249:1–35

Smythe DJ, Brenan JM (2015) Cerium oxidation state in silicate melts: combined fO2, temperature and compositional effects. Geochim Cosmochim Acta 170:173–187

Streck MJ, Dilles JH (1998) Sulfur evolution of oxidized arc magmas as recorded in apatite from a porphyry copper batholith. Geology 26:523–526

Thomas JB, Bodnar RJ, Shimizu N, Chesner CA (2003) Melt Inclusions in Zircon. Rev Mineral Geochemistry 53:63–87

Trail D, Warson EB, Taiby ND (2012) Ce and Eu anomalies in zircon as proxies for the oxidation state of magmas. Geochim Cosmochim Acta 97:70–87

Van Lichtervelde M, Holtz F, Dziony W, et al (2011) Incorporation mechanisms of Ta and Nb in zircon and implications for pegmatitic systems. Am Mineral 96:1079–1089. doi: 10.2138/am.2011.3650

Wainwright AJ, Tosdal RM, Wooden JL, et al (2011) U-Pb (zircon) and geochemical constraints on the age, origin, and evolution of Paleozoic arc magmas in the Oyu Tolgoi porphyry Cu-Au district, southern Mongolia. Gondwana Res 19:764–787

Wang F, Liu SA, Li S, He Y (2013) Contrasting zircon Hf-O isotopes and trace elements between ore-bearing and ore-barren adakitic rocks in central-eastern China: implications for genetic relation to Cu-Au mineralization. Lithos 15:97–111

Wang R, Richards JP, Hou ZQ, et al (2014) Increased magmatic water content-the key to Oligo-Miocene porphyry Cu-Mo±Au formation in the eastern Gangdese belt, Tibet. Econ Geol 195:1315–1339

Ward SR (2008) Isotope geochemistry of zircons from the Guichon Batholith, Highland Valley Copper deposit: Southern British Columbia: Relationship between Ce4+/Ce3+ in zircon, oxidation state in magmas and ore genesis. unpublished BSc. thesis, Department of Earth Sciences, Carleton University, Ottawa, ON

Watson EB, Harrison TM (1983) Zircon saturation revisited: Temperature and composition effects in a variety of crustal magma types. Earth Planet Sci Lett 64:295–304

Watson EB, Wark DA, Thomas JB (2006) Crystallization thermometers for zircon and rutile. Contrib to Mineral Petrol 151:413–433

Whalen JB, Davis WJ, Anderson RA (2017) Temporal and geochemical evolution of the Guichon Creek Batholith and Highland Valley porphyry copper district, British Columbia: implications for generation and tectonic setting of porphyry systems. Geol Surv Canada, Open File 8334

Wiedenbeck M, Hanchar JM, Peck WH, et al (2004) Further Characterisation of the 91500 Zircon Crystal. Geostand Geoanalytical Res 28:9–39

Wilke M, Behrens H (1999) The dependence of the partitioning of iron and europium between plagioclase and hydrous tonalitic melt on oxygen fugacity. Contrib to Mineral Petrol 137:102–114

Wooden JL, Mazdab FK, Barth AP, et al (2006) Temperatures (Ti) and compositional characteristics of zircon: Early observations using high mass resolution on the USGS Stanford SHRIMP-RG. Geochim Cosmochim Acta Suppl 70:707

Zhong S, Seltmann R, Qu H, Song Y (2019) Characterization of the zircon Ce anomaly for estimation of oxidation state of magmas: a revised Ce/Ce* method. Mineral Petrol 113:755–763

Figure Captions

Figure 1. Simplified geologic map of the Guichon Creek batholith (GCB) and the surrounding region with locations of ore deposits and prospects. Modified after Massey et al. (2005) and McMillan et al. (2009). Inset denotes the location of Figure 2.

Figure 2. Geologic map of Guichon Creek batholith and Highland Valley district modified after McMillan et al. (2009) and Lesage et al. (2019) with locations of samples used in this study. Ages from D'Angelo et al. (2017) except Gump Lake stock (this study). FQPC = feldspar and quartz crowded porphyry dike, "S&P" = salt and pepper, QFPQ = quartz-feldspar-phyric, quartz-rich, porphyry dike.

Figure 3. Reflected light, transmitted light, and cathodoluminescence images for selected zircon grains analyzed for this study. Images used to characterize zircon from Guichon Creek batholith and identify inclusions, growth zoning, and potential cores. Samples include Gump Lake stock-KB132 (A. B. C.); Guichon subfacies-SM059 (D. E. F.); Bethsaida facies-SB217 (G. H. I.); QFPQ-MA121 (J. K. L.). Laser ablation spot size 47 μm. Hf – concentration in ppm, Eu* = Eu/Eu_N*, Temp – calculated Ti[49] temperature in °C.

Figure 4. Geochemical plots of whole-rock data for the Guichon Creek Batholith samples. A. Plot of SiO_2 vs. Al_2O_3. B. Plot of molar Al/Ti vs. Zr. C. Chondrite-normalized rare earth element plot (after McDonough and Sun, 1995). D. Primitive mantle normalized multi-element plot. Sample data symbols the same for all plots, smaller data symbols of Guichon Creek batholith from D'Angelo et al. (2017).

Figure 5. Uranium-lead concordia plot for Gump Lake stock sample KB132. Shaded ellipses represent zircon fractions used for determining weighted mean U-Pb age; dashed ellipses represent zircon interpreted as antycrystic.

Figure 6. Zircon composition plots of Hf ppm vs Eu/Eu_N* for A. Gump Lake stock. B. Early Guichon Creek facies. C. Middle Bethlehem facies. D. dikes from Bethlehem pit, including Bethlehem porphyry, late Jersey stock, and FQPC (ppy = porphyry). E. Late Guichon Creek facies from the core of the batholith. F. Late syn- to post-mineral "S&P" Bethsaida and quartz-feldspar-phyric, quartz-rich porphyry dike. Dashed line denotes approximate break between the field of normal magmatic evolution with little to no SO_2 gas separation (below line) and field of elevated oxidation state due to increased fluid and gas loss (Dilles et al. 2015).

Figure 7. Zircon composition plots of Hf ppm vs. calculated Ti-in-zircon Temperature (°C) for A. Early Guichon Creek facies including Gump Lake stock. B. Middle Guichon Creek facies including dikes from Bethlehem pit. C. Late Guichon Creek facies from the core of the batholith. D. Late syn- to post-mineral "S&P" Bethsaida dike and quartz-feldspar-phyric porphyry dike. Temperature calculations after Watson et al. (2006), corrected to an activity of $TiO_2 \approx 0.5$-0.7, to reflect titanite and titanomagnetite saturation (Clairborne et al. 2006; Ferry and Watson, 2007). Solid black lines represent linear regression lines highlighting temperatures decrease with increasing Hf content for most of the samples consistent with cooling during crystallization (Dilles et al. 2015; Lee et al. 2017b).

Figure 8. Plots of zircon Hf vs. Y (A.) and Hf vs Nb/Ta (B.) values for the Gump Lake stock, early Guichon Creek facies, Bethlehem facies and dikes, late Skeena and Bethsaida, and late dikes.

Figure 9. Plots of normalized zircon concentration for the Guichon Creek batholith. A. Ce vs. Sm.., B. Ce vs. Nd.C.Yb vs. Gd . Symbols the same as in Figure 8.

Figure 10. Trace element ratio plots for the Guichon Creek batholith zircon. A. Th/U vs $Yb/Gd_{N.}$ B. Sm/Ce_N vs $Yb/Gd_{N.}$ C. Th/U vs Hf/Y. D. $(Ce/Nd_N)/Y$ vs Eu/Eu_N*. Fractionated melting paths and mixing tie lines after Lee et al. (2017b).

Figure 11. Plot of normalized zircon europium and cerium anomalies from the Guichon Creek batholith samples.Fertile systems generally plot above 0.4 Eu/Eu_N* and have a large variability of Ce/Ce_N* values but typically above 100.

Figure 12. Distribution plots for zircon Eu/Eu_N* values from Guichon Creek batholith samples, modified after Lee et al. (2017a). Number of analyses per sample labeled above each plot, average value given by black dot, GCB – Guichon Creek batholith.

Figure 13. Model of formation for the Guichon Creek batholith and Highland Valley deposit modified after D'Angelo et al. 2017. A. Earliest magmatic emplacement of the Gump Lake stock at ~218 Ma forming a potential pathway for later Guichon Creek intrusives. B. Early emplacement of Border facies with the assimilation of country Nicola Group volcanic and sedimentary rocks, followed by the Highland Valley facies with inward crystallization forming the Guichon and Chataway subfacies with possible fluid enrichment due to Bethlehem magma. C. Emplacement of the vapor-rich Bethlehem facies, followed by intrusion of porphyry dikes and stocks causing the mineralization and brecciation at the Bethlehem deposit. D. Continued emplacement of the highly oxidized Skeena and Bethsaida facies priming the region for large mineralized ore deposits at Valley, Lornex, Highmont, and J.A. following the intrusion of a new mafic(?) melt forming a volatile-rich magma. Final crystallization of this volatile-melt formed the late post-mineral dikes and aplites. GCB = Guichon Creek batholith; V-L-H = Valley-Lornex-Highmont; Beth = Bethlehem deposit; Beth ppy = Bethlehem porphyry; "S&P" Bda = 'salt & pepper' Bethsaida.

Table Titles

Table 1. U-Th-Pb isotopic data for Gump Lake stock sample KB132

Table 2. Summary of zircon composition for the Gump Lake and Guichon Creek intrusions

Electronic supplementary material

ESM Figure S1. Transmitted, reflected, and cathodoluminescent images of all zircon grains analyzed from the Guichon Creek batholith and Highland Valley copper rocks

ESM Figure S2. Comparison plots of normalized europium and cerium anomalies from the Guichon Creek batholith, south-central Canada determined by A. method of Dilles et al. (2017) and Loader et al. (2017) and B. exponential power function as described by Zhong et al. (2019) and modified for this study (see ESM Table S5 for methods and results).

ESM Table S1. Selected CA-TIMS U-Pb ages from Guichon Creek batholith

ESM Table S2. Whole rock major and trace element chemistry for Guichon Creek batholith samples

ESM Table S3. Trace element composition of zircon from LA-ICP-MS analytical runs of Highland Valley Copper and Guichon Creek batholith samples and standards

ESM Table S4. Zircon composition for Gump Lake stock and Guichon Creek batholith rocks

ESM Table S5. Ce/Ce_C* calculation of Guichon Creek batholith zircon grains

Table 1. U-Th-Pb isotopic data for Gump Lake stock sample KB132[1]

Composition[2]								Radiogenic Isotope Ratios[3]									Isotopic Ages[4]					
Wt. (mg)	U (ppm)	Pb (ppm)	Th/U	$^{206}Pb*x10^{-13}$ mol	^{206}Pb mol %	Pb*/Pbc	Pbc (pg)	$^{206}Pb/^{204}Pb$	$^{208}Pb/^{206}Pb$	$^{207}Pb/^{206}Pb$	2s	$^{207}Pb/^{235}U$	2s	$^{206}Pb/^{238}U$	2s	corr. coef.	$^{207}Pb/^{206}Pb$	2s	$^{207}Pb/^{235}U$	2s	$^{206}Pb/^{238}U$	2s
0.0082	146	5.3	0.372	1.7246	98.63%	21	1.97	1345	0.118	0.050561	0.349	0.239743	0.400	0.034389	0.111	0.566	220.89	8.08	218.21	0.79	217.96	0.24
0.0044	387	13.4	0.325	2.4229	99.67%	87	0.66	5563	0.103	0.050530	0.134	0.239737	0.214	0.034410	0.133	0.798	219.44	3.10	218.21	0.42	218.09	0.29
0.0048	219	7.7	0.351	1.5135	99.48%	56	0.65	3575	0.112	0.050475	0.199	0.239917	0.285	0.034473	0.169	0.729	216.93	4.60	218.35	0.56	218.48	0.36
0.0069	259	9.1	0.347	2.5845	99.54%	63	0.99	4006	0.110	0.050436	0.180	0.240140	0.277	0.034532	0.179	0.768	215.15	4.18	218.54	0.54	218.85	0.38
0.0077	256	9.0	0.401	2.8448	99.74%	112	0.62	7026	0.127	0.050456	0.127	0.240539	0.330	0.034576	0.289	0.924	216.05	2.94	218.86	0.65	219.12	0.62

[1] single grain TIMS zircon analyses; first two rows used in calculated age of 218.01 ± 0.18 Ma, see Figure X

[2] Nominal weights, U, and Pb concentration estimated from grain dimensions. Pb* and Pbc represent radiogenic and common Pb, respectively

[3] Ratios corrected for fractionation, spike, and up to 1pg common Pb was assumed to be procedural blank: $^{206}Pb/^{204}Pb$ = 18.50 ± 1.0%; $^{207}Pb/^{204}Pb$ = 15.50 ± 1.0%;
All errors propagated following algorithms of Schmitz and Schoene (2007) and Crowley et al. (2007)

[4] Age calculations are based on the decay constants of Jaffey et al. (1971) and listed as Ma. $^{206}Pb/^{238}U$ and $^{207}Pb/^{206}Pb$ ages corrected for initial disequilibrium in $^{230}Th/^{238}U$ using Th/U [magma] = 3

Table 2. Summary of zircon composition for the Gump Lake and Guichon Creek intrusions

Magma Pulse(s)[1]	Rock facies/type	Age (Ma)[2]	Zircon Eu/Eu_N*		Zircon Temp C°		Y	Nb/Ta	Yb/Gd	Note
			Range	Mean	Max	Min	Mean	Mean	Range	
Pre-MGCB [8]	Gump Lake stock	~218	0.22-0.38	0.27	773	660	951	4.59	38-58	Initial barren quarz monzonite intrusion
Early-MGCB [69]	Border & Guichon	~211.0-210.5	0.22-0.56	0.31	954	694	670	0.50	12-38	Mafic pulse(s) initiated from lower crust MASH
Early-MGCB [55]	Chataway	~210.5	0.32-0.72	0.40	800	692	512	0.37	13-45	Rim zircon composition suggests presence of titanite with amphibole + apatite during crystalization
Mid-MGCB [46]	Bethlehem	~209.5	0.34-0.65	0.47	900	675	476	0.48	13-41	Oxidized and hydrous magma
Mid-MGCB [98]	Bethlehem dikes & stocks	~209	0.30-0.73	0.50	795	605	460	0.40	13-47	Pre- to post-mineral dikes and stocks source of mineralization at Bethlehem deposit
Late-MGCB [64]	Skeena & Bethsaida	~208.8-208.5	0.39-0.74	0.51	784	610	590	0.90	20-51	Evolved and oxidized upper magma chamber intrusives
Post-MGCB [67]	"S&P" Bethsaida & QFPQ	~208-207	0.19-0.73	0.27	808	597	1680	8.98	21-52	Syn-mineral dikes from volatile from late mafic(?) intrusion into upper chamber, coeval with large fluid release and formation of V-L-H Cu deposits[3], followed by late filter pressing of magma chamber causing emplacement of post-mineral dikes

[1]Magmatic pulse discussed in text and based on age, whole rock composition, and zircon composition. Number of analyses per row given in brackets. MGCB = Main Guichon Creek batholith intrusion event

[2]Approximate age based on U-Pb CA-TIMS dating, see Table 1

[3]V - Valley deposit, L - Lornex deposit, H - Highmont deposit

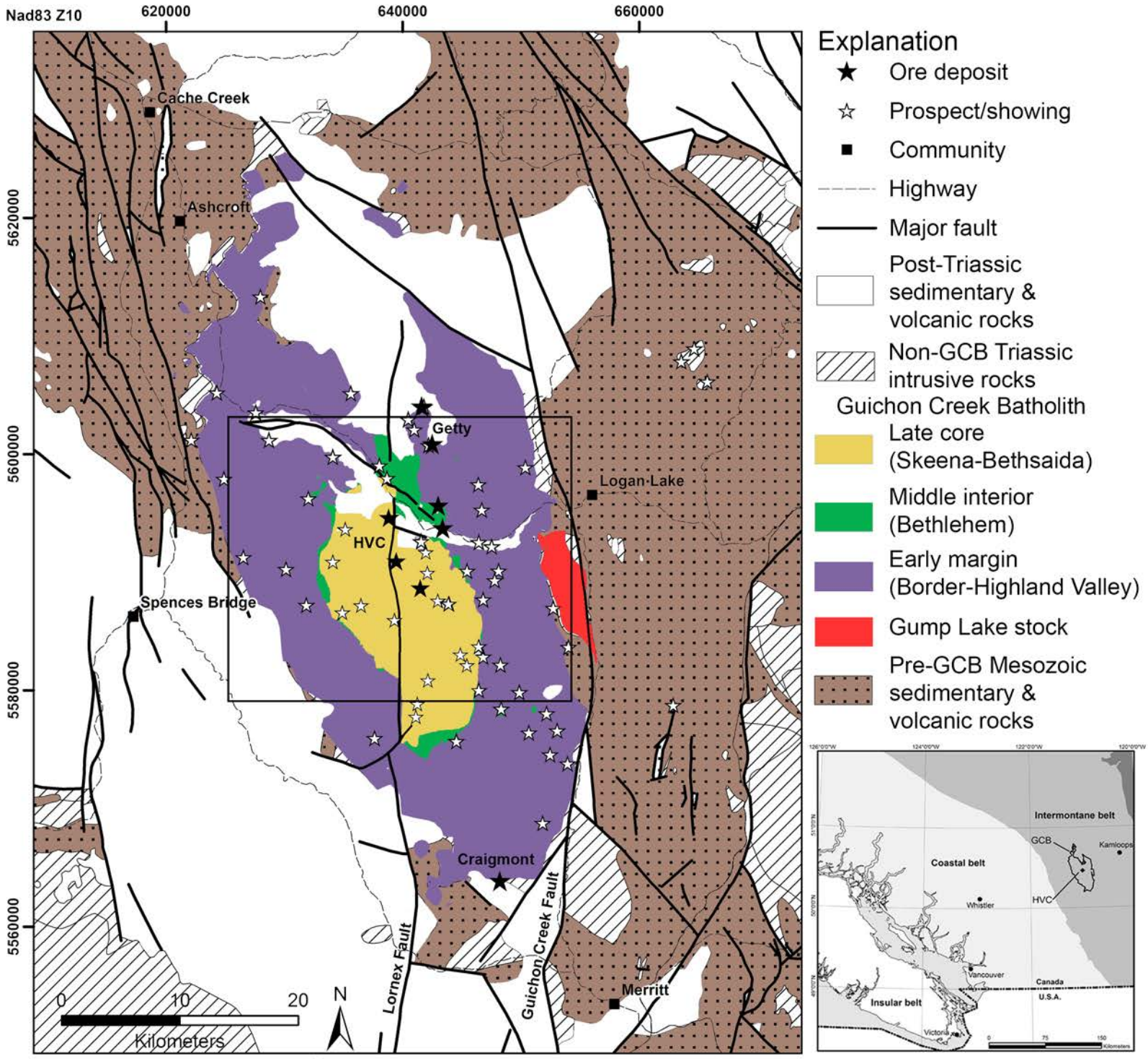
Nad83 Z10
620000
640000
660000
5620000
5600000
5580000
5560000
Cache Creek
Ashcroft
Getty
Logan Lake
HVC
Spences Bridge
Craigmont
Merritt
Lornex Fault
Guichon Creek Fault
0
10
20
Kilometers
N
Explanation
Ore deposit
Prospect/showing
Community
Highway
Major fault
Post-Triassic sedimentary & volcanic rocks
Non-GCB Triassic intrusive rocks
Guichon Creek Batholith
Late core (Skeena-Bethsaida)
Middle interior (Bethlehem)
Early margin (Border-Highland Valley)
Gump Lake stock
Pre-GCB Mesozoic sedimentary & volcanic rocks
Intermontane belt
GCB
Kamloops
Coastal belt
Whistler
HVC
Vancouver
Canada
U.S.A.
Insular belt
Victoria

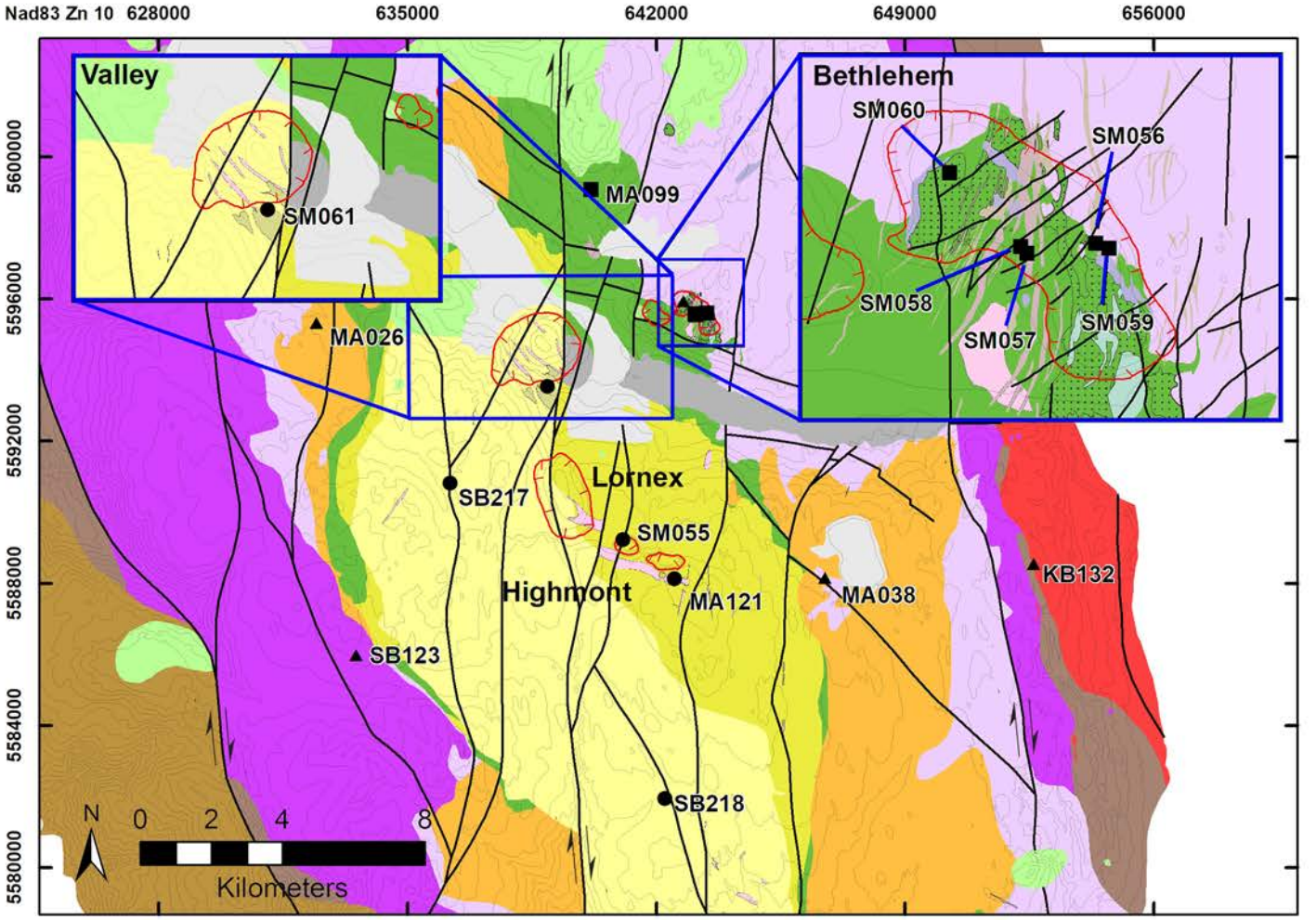

Explanation

Sample Locations ▲ Early ■ Mid ● Late — HVC pit outline — Major fault

Geology

Recent

- Anthropogenic

Tertiary

- Highland Valley Group
- Kamloops Group

Cretaceous

- Spences Bridge Group

Triassic - Guichon Creek Batholith

Early 210.4 to 211.0 Ma

- Chataway sub-facies
- Guichon sub-facies
- Border facies

Mid 208.5 to 209.8 Ma

- Breccias
- FQPC
- Jersey stock
- Bethlehem porphyry
- Bethlehem facies

Late 206.9 - 208.5 Ma

- Late porphyry dikes includes QFPQ
- "S&P" Bethsaida porphyry
- Bethsaida facies
- Skeena facies

Triassic - Pre-GCB

- Gump Lake stock - 218 Ma
- Nicola Group

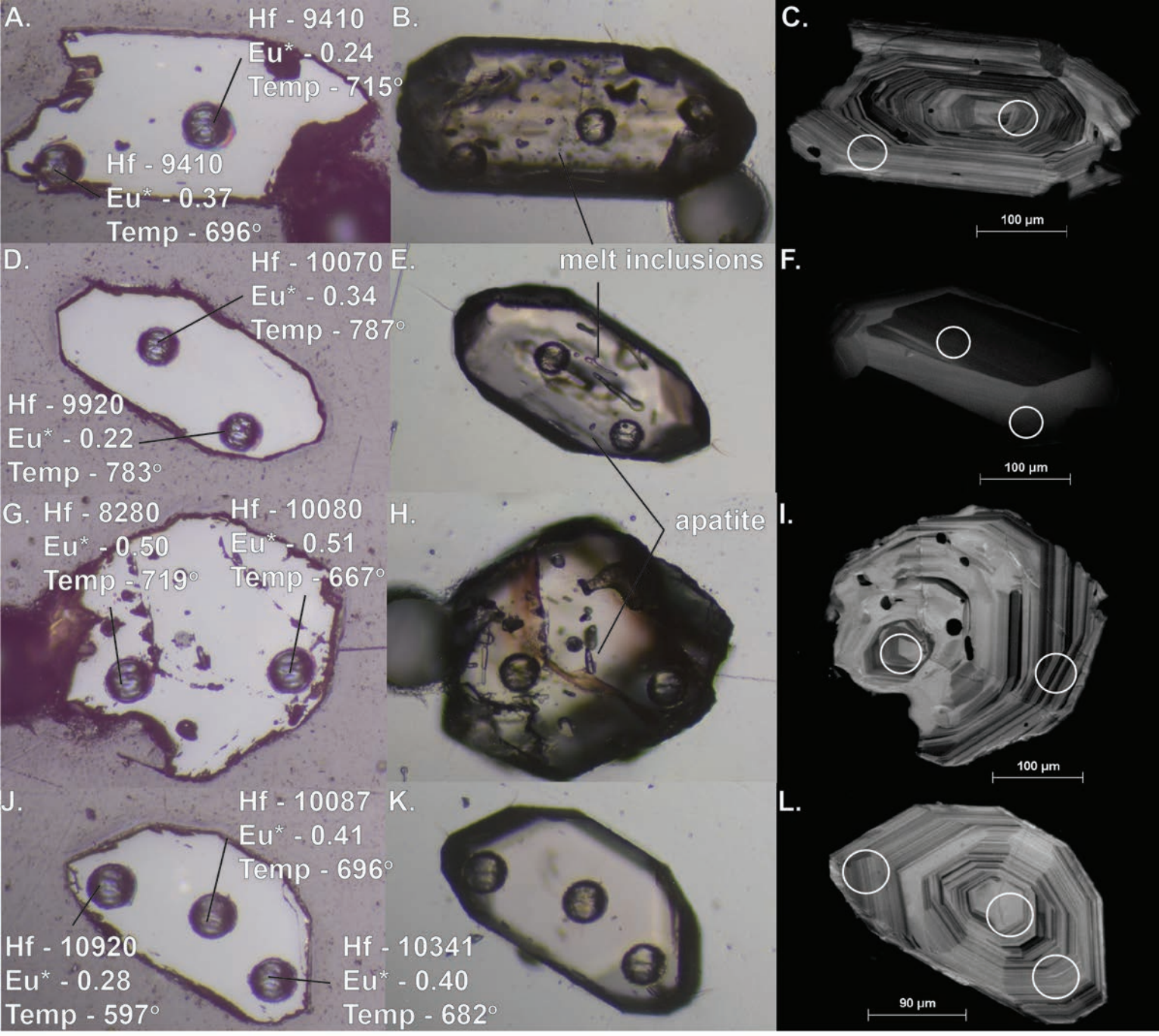

Reflected Light **Transmitted Light** **Cathodoluminescence**

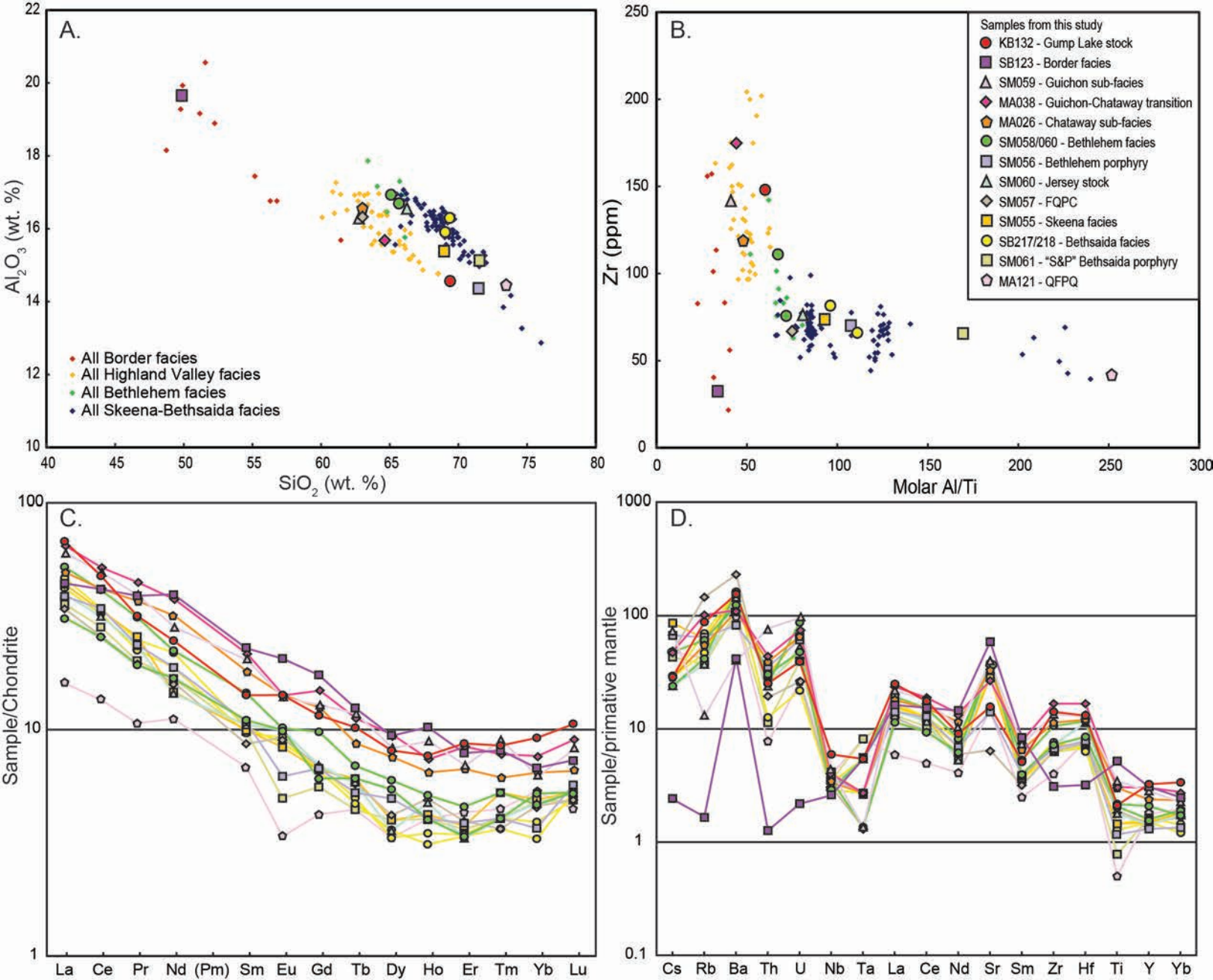
A.
Al_2O_3 (wt. %)
SiO_2 (wt. %)
All Border facies
All Highland Valley facies
All Bethlehem facies
All Skeena-Bethsaida facies
B.
Zr (ppm)
Molar Al/Ti
Samples from this study
KB132 - Gump Lake stock
SB123 - Border facies
SM059 - Guichon sub-facies
MA038 - Guichon-Chataway transition
MA026 - Chataway sub-facies
SM058/060 - Bethlehem facies
SM056 - Bethlehem porphyry
SM060 - Jersey stock
SM057 - FQPC
SM055 - Skeena facies
SB217/218 - Bethsaida facies
SM061 - "S&P" Bethsaida porphyry
MA121 - QFPQ
C.
Sample/Chondrite
La Ce Pr Nd (Pm) Sm Eu Gd Tb Dy Ho Er Tm Yb Lu
D.
Sample/primative mantle
Cs Rb Ba Th U Nb Ta La Ce Nd Sr Sm Zr Hf Ti Y Yb

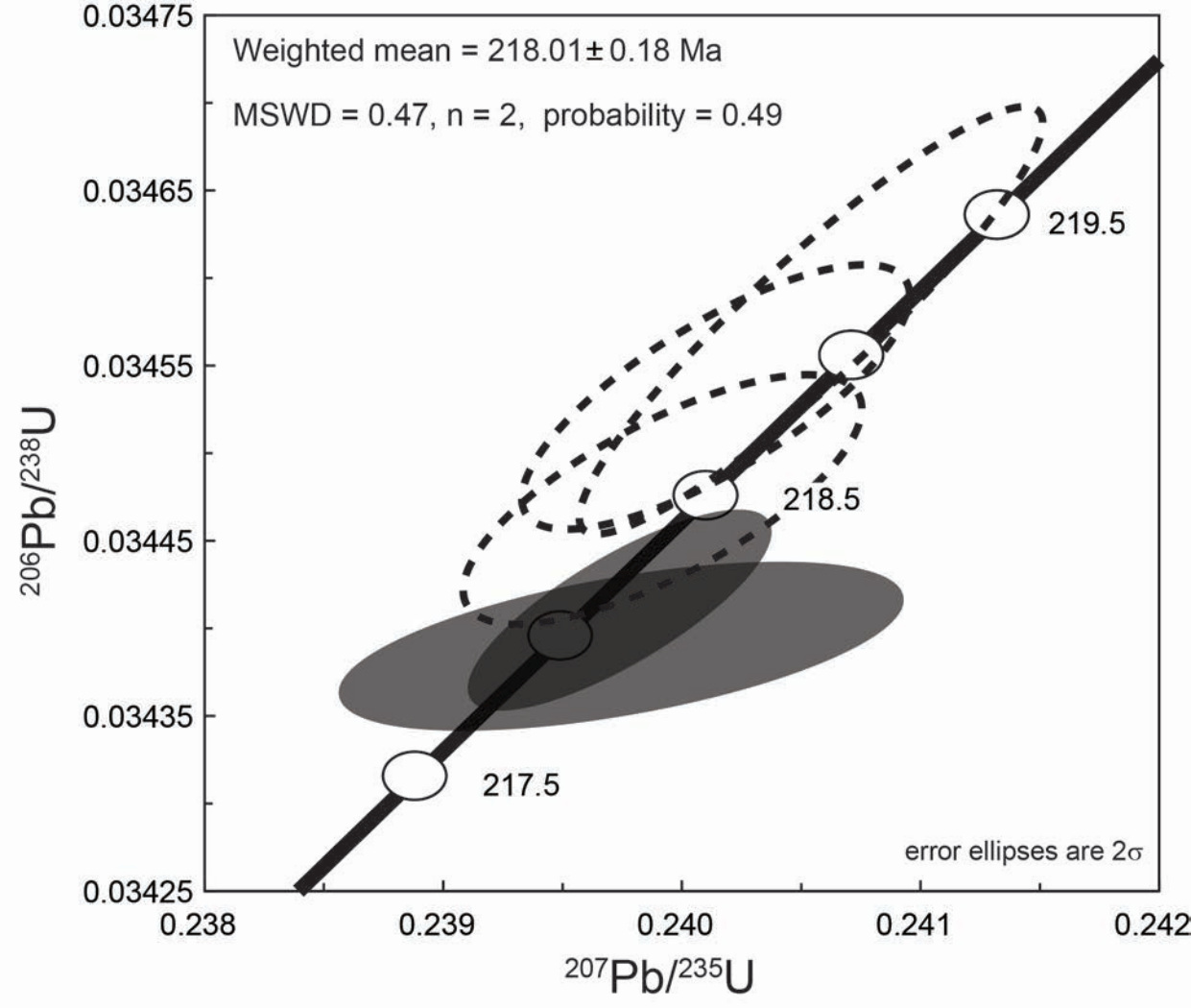
Weighted mean = 218.01± 0.18 Ma
MSWD = 0.47, n = 2, probability = 0.49
219.5
218.5
217.5
error ellipses are 2σ
0.03475
0.03465
0.03455
0.03445
0.03435
0.03425
0.238
0.239
0.240
0.241
0.242
206Pb/238U
207Pb/235U

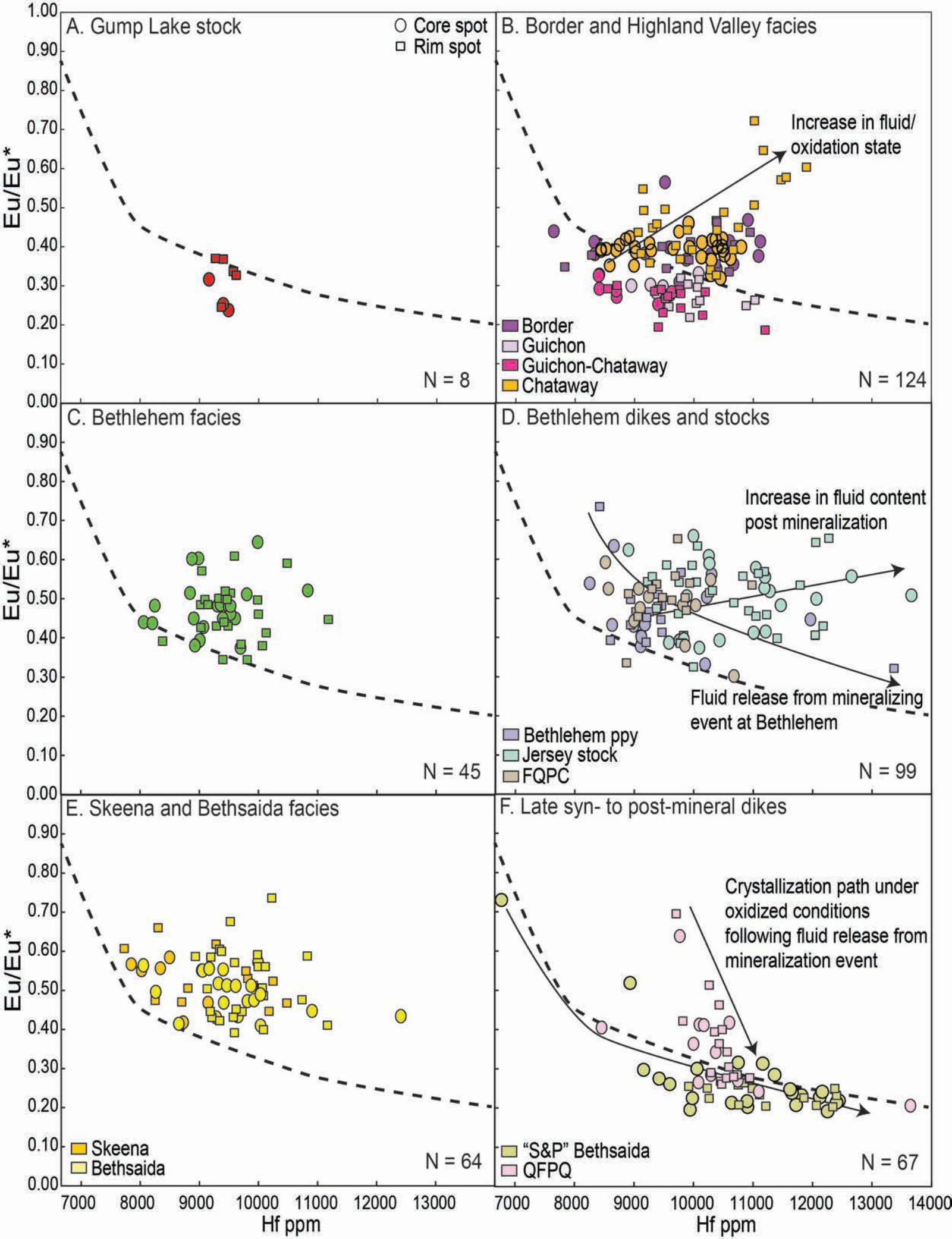
A. Gump Lake stock
Core spot
Rim spot
N = 8
B. Border and Highland Valley facies
Increase in fluid/
oxidation state
Border
Guichon
Guichon-Chataway
Chataway
N = 124
C. Bethlehem facies
N = 45
D. Bethlehem dikes and stocks
Increase in fluid content
post mineralization
Fluid release from mineralizing
event at Bethlehem
Bethlehem ppy
Jersey stock
FQPC
N = 99
E. Skeena and Bethsaida facies
Skeena
Bethsaida
N = 64
F. Late syn- to post-mineral dikes
Crystallization path under
oxidized conditions
following fluid release from
mineralization event
"S&P" Bethsaida
QFPQ
N = 67
Eu/Eu*
Hf ppm
0.00
0.10
0.20
0.30
0.40
0.50
0.60
0.70
0.80
0.90
1.00
7000
8000
9000
10000
11000
12000
13000
14000

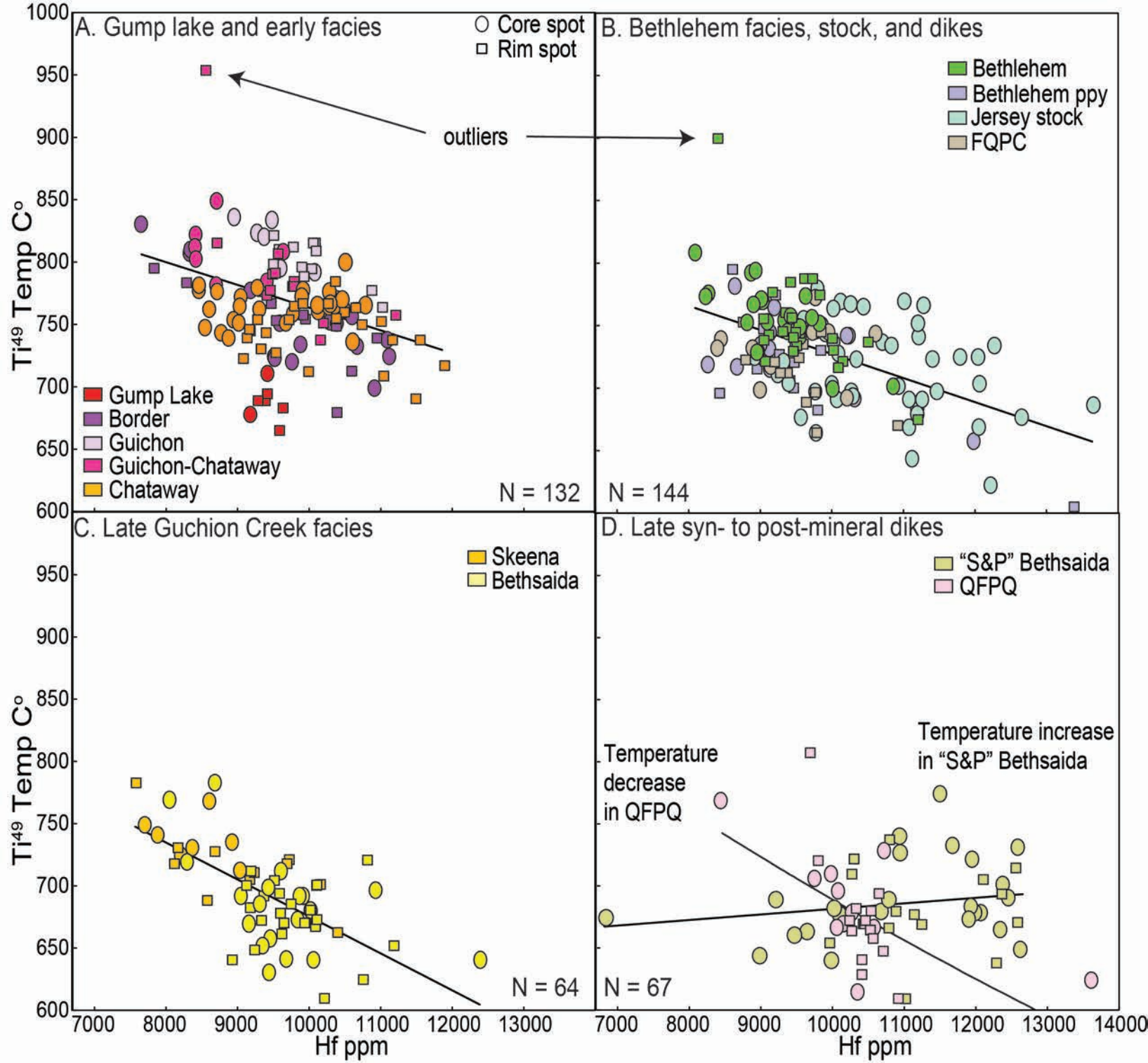
A. Gump lake and early facies
Core spot
Rim spot
outliers
Gump Lake
Border
Guichon
Guichon-Chataway
Chataway
N = 132
B. Bethlehem facies, stock, and dikes
Bethlehem
Bethlehem ppy
Jersey stock
FQPC
N = 144
C. Late Guchion Creek facies
Skeena
Bethsaida
N = 64
D. Late syn- to post-mineral dikes
"S&P" Bethsaida
QFPQ
Temperature decrease in QFPQ
Temperature increase in "S&P" Bethsaida
N = 67
Ti49 Temp C°
Hf ppm
1000
950
900
850
800
750
700
650
600
7000
8000
9000
10000
11000
12000
13000
14000

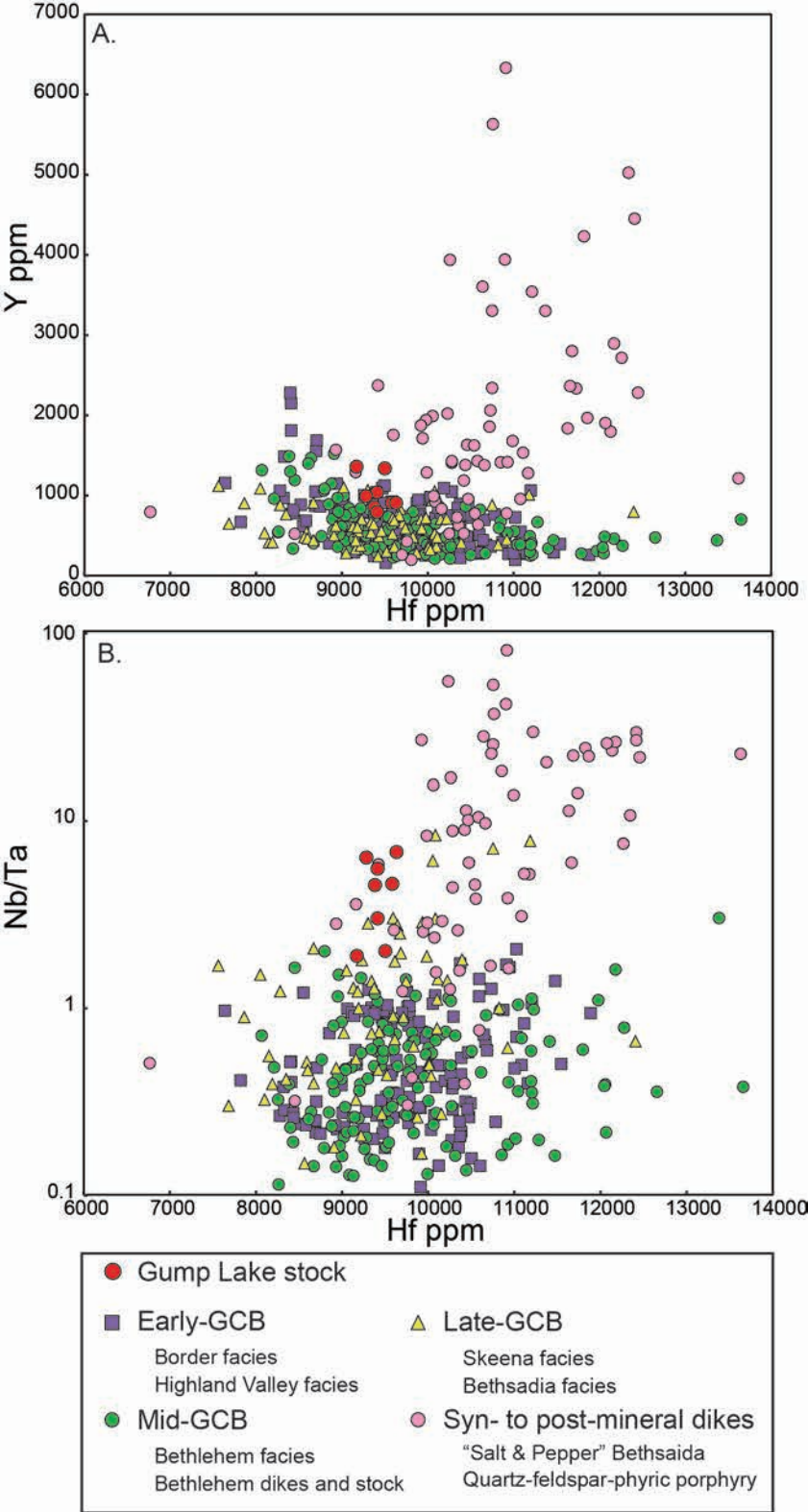
A.
Y ppm
Hf ppm
B.
Nb/Ta
Hf ppm
Gump Lake stock
Early-GCB
Border facies
Highland Valley facies
Late-GCB
Skeena facies
Bethsadia facies
Mid-GCB
Bethlehem facies
Bethlehem dikes and stock
Syn- to post-mineral dikes
"Salt & Pepper" Bethsaida
Quartz-feldspar-phyric porphyry

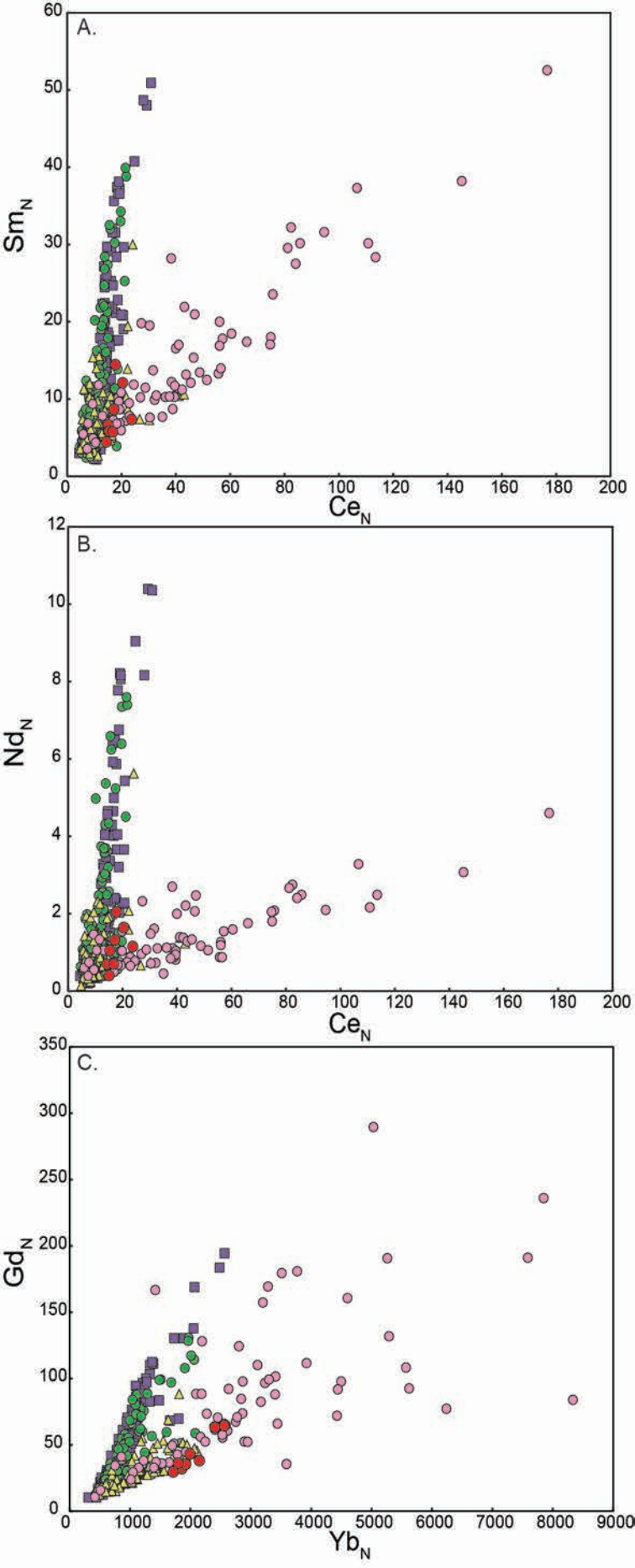
A.
Sm_N
Ce_N
B.
Nd_N
Ce_N
C.
Gd_N
Yb_N

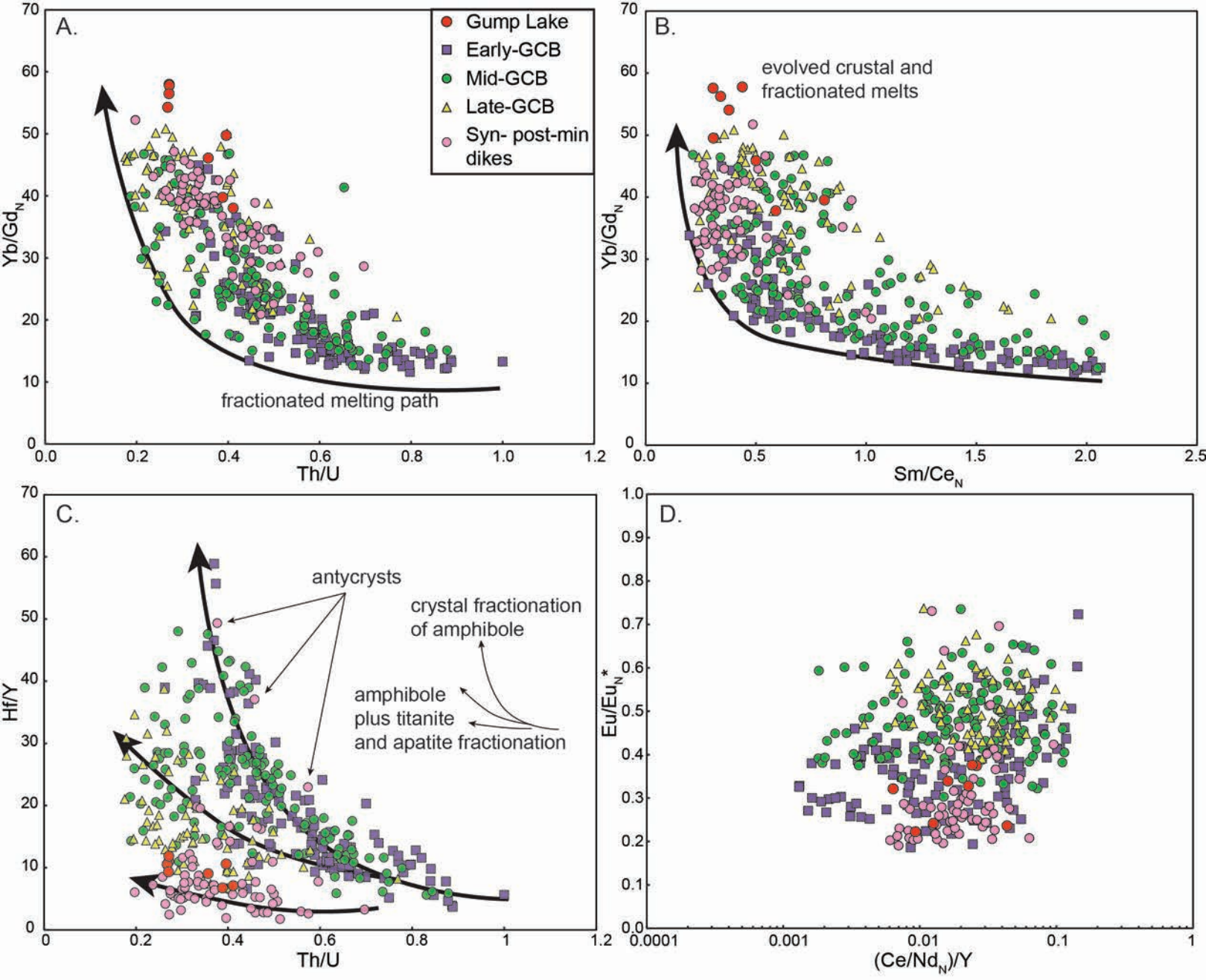
A.
Gump Lake
Early-GCB
Mid-GCB
Late-GCB
Syn- post-min dikes
fractionated melting path
Yb/Gd$_N$
Th/U
B.
evolved crustal and fractionated melts
Yb/Gd$_N$
Sm/Ce$_N$
C.
antycrysts
crystal fractionation of amphibole
amphibole plus titanite and apatite fractionation
Hf/Y
Th/U
D.
Eu/Eu$_N$*
(Ce/Nd$_N$)/Y

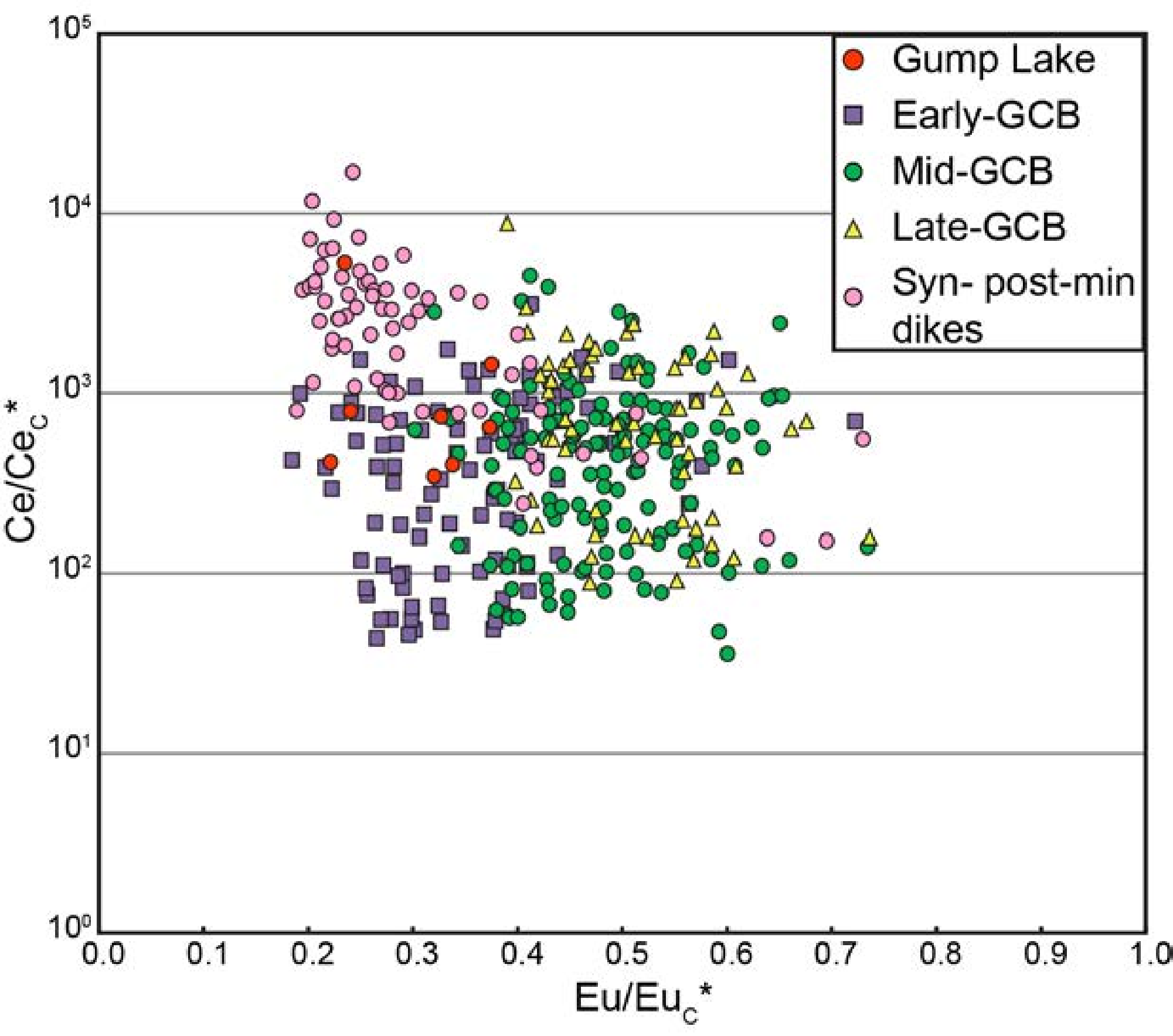
Gump Lake
Early-GCB
Mid-GCB
Late-GCB
Syn- post-min dikes
10^5
10^4
10^3
10^2
10^1
10^0
Ce/Ce$_C$*
0.0
0.1
0.2
0.3
0.4
0.5
0.6
0.7
0.8
0.9
1.0
Eu/Eu$_C$*

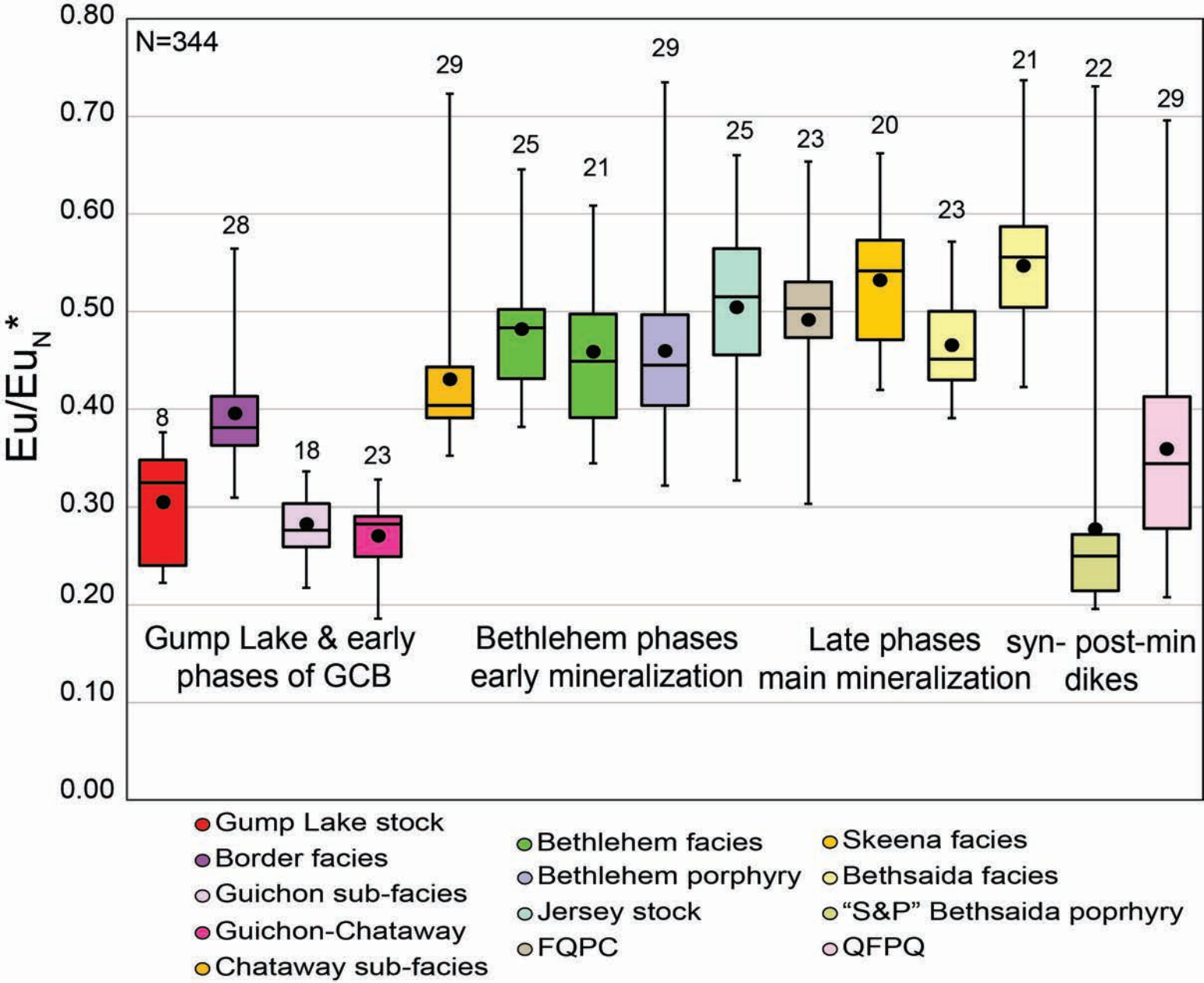
N=344
Eu/Eu$_N$*
0.80
0.70
0.60
0.50
0.40
0.30
0.20
0.10
0.00
8
28
18
23
29
25
21
29
25
23
20
23
21
22
29
Gump Lake & early phases of GCB
Bethlehem phases early mineralization
Late phases main mineralization
syn- post-min dikes
Gump Lake stock
Border facies
Guichon sub-facies
Guichon-Chataway
Chataway sub-facies
Bethlehem facies
Bethlehem porphyry
Jersey stock
FQPC
Skeena facies
Bethsaida facies
"S&P" Bethsaida poprhyry
QFPQ

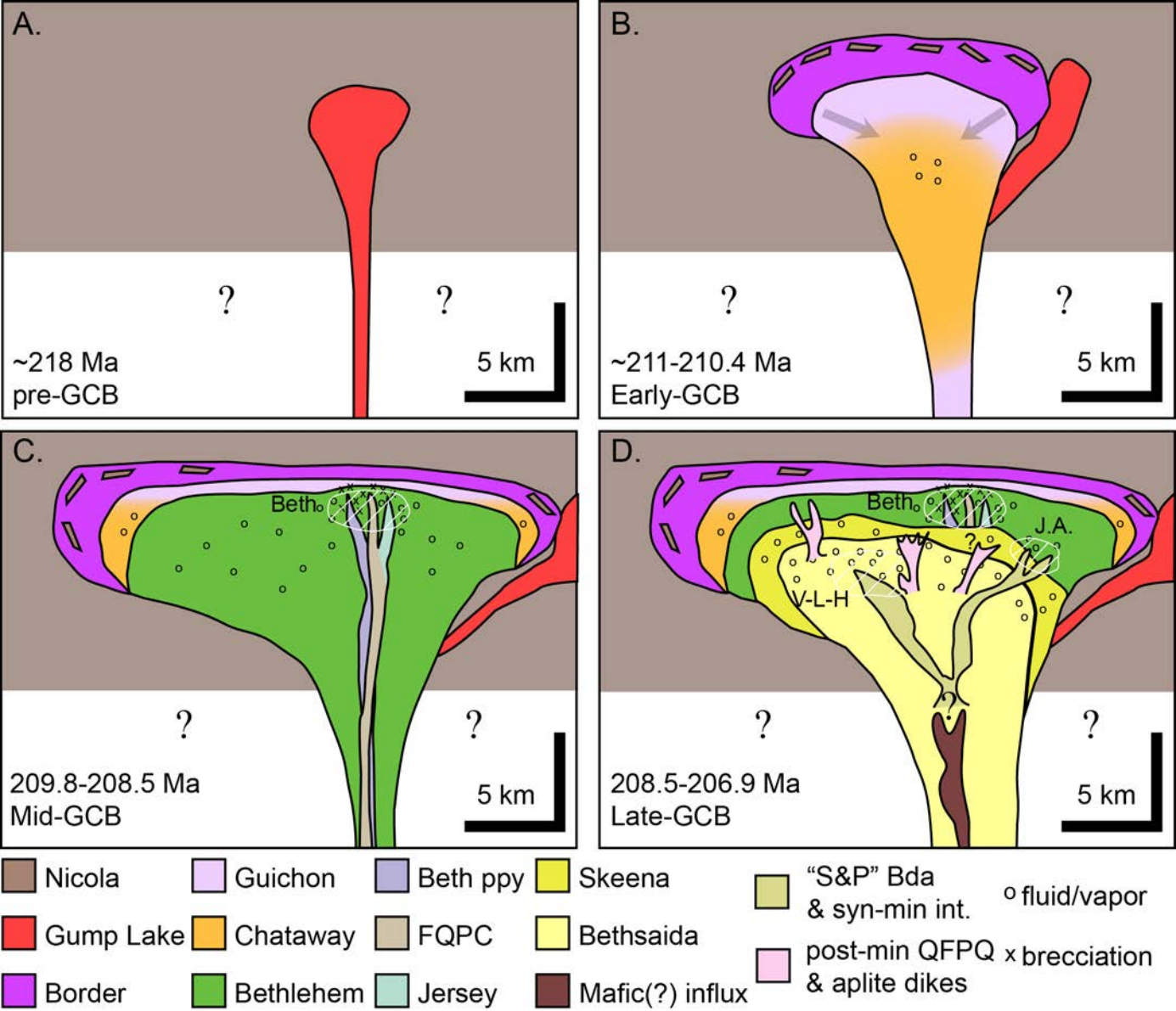
A.
?
?
~218 Ma
pre-GCB
5 km
B.
?
?
~211-210.4 Ma
Early-GCB
5 km
C.
Beth
?
?
209.8-208.5 Ma
Mid-GCB
5 km
D.
Beth
J.A.
V-L-H
?
?
?
208.5-206.9 Ma
Late-GCB
5 km
Nicola
Gump Lake
Border
Guichon
Chataway
Bethlehem
Beth ppy
FQPC
Jersey
Skeena
Bethsaida
Mafic(?) influx
"S&P" Bda
& syn-min int.
post-min QFPQ
& aplite dikes
o fluid/vapor
x brecciation